

Probabilistic machine learning of relaxation time distributions in spectral induced polarization

Charles L. Bérubé*, Sébastien Gagnon*, Lahiru M.A. Nagasingha*, Jean-Luc Gagnon†, E. Rachel Kenko*, Reza Ghanati‡, Frédérique Baron§

* *Civil, geological and mining engineering department*

† *Engineering physics department*

Polytechnique Montréal

C.P. 6079, succ. Centre-ville

Montréal QC Canada H3C 3A7

‡ *Department of Earth Physics, Institute of Geophysics*

University of Tehran

Tehran Iran 14359-44411

§ *Physics department*

Université de Montréal

C.P. 6128, succ. Centre-ville

Montréal QC Canada H3C 3J7

(March 17, 2026)

Submitted to *Geophysics*

Running head: **Probabilistic SIP decomposition**

Probabilistic machine learning of relaxation time distributions in spectral induced polarization

(March 17, 2026)

Submitted to *Geophysics*

Running head: Probabilistic SIP decomposition

ABSTRACT

Debye decomposition methods are widely used to interpret spectral induced polarization (SIP) data and to recover the relaxation time distribution (RTD) of geomaterials. However, SIP interpretation remains challenging for heterogeneous data sets because conventional decomposition methods treat each spectrum independently and provide limited uncertainty quantification. A probabilistic machine learning method is introduced to infer continuous RTD directly from complex resistivity spectra, using a combined laboratory and field data set comprising 140 SIP measurements of granular mixtures, rock cores, field surveys, and cementitious materials. The approach relies on a conditional variational autoencoder (CVAE) that performs decomposition at the data set level and learns a shared inverse mapping from complex resistivity spectra to probabilistic RTD expressed as Gaussian mixtures. The CVAE reproduces measured spectra with global errors below 0.53% and 0.45% over the full frequency range for the real and imaginary components, respectively. Dominant relaxation modes are recovered consistently, and both the total chargeability and the mean relaxation time show strong correlations with polarizable grain content and grain size, respectively, with coefficients of determination up to 0.95. Jacobian-based sensitivity analysis shows that the placement, width, and relative weighting of relaxation modes contribute to approximately 89% of the decomposition process. In contrast, the total chargeability contributes to 10% and the resistivity scaling parameter less than 1%. Latent variables learned by the CVAE organize SIP data into a structured space where sample populations naturally cluster without supervision. Compared to the chargeability and relaxation time domain, a two-dimensional projection of the latent variables improves the Davies–Bouldin clustering index by nearly a factor of three. The results demonstrate that probabilistic machine learning of RTD provides a new, accurate, and interpretable framework for SIP data analysis across diverse geomaterials.

INTRODUCTION

Spectral induced polarization (SIP) measures the frequency dispersion of the electrical resistivity of geomaterials and characterizes their ability to temporarily and reversibly store energy. The idea of a relaxation time distribution (RTD) is a central element in the interpretation of dielectric data and, by extension, in the analysis of SIP measurements. Early evidence for this concept appears in Yager (1936), which demonstrates that dielectric materials exhibit a continuous range of relaxation processes. In Morgan and Lesmes (1994), a major methodological step is achieved through a stable numerical procedure that uses a logarithmic transformation to recover the RTD of dielectric spectra. Nordsiek and Weller (2008) then adapts the RTD concept to complex resistivity spectra, and Zorin (2015) offers a physical justification for interpreting SIP data using Debye relaxation models. These contributions provide the conceptual and algorithmic foundations for modern Debye decomposition (DD) techniques.

Several studies extend the foundations of DD by developing deterministic and stochastic inversion strategies. Among them, Keery et al. (2012) introduces a probabilistic formulation of DD using a Markov chain Monte Carlo sampler, and Florsch et al. (2014) uses an L-curve regularization scheme to obtain stable RTD solutions. Ustra et al. (2016) proposes an alternative formulation of the DD for complex conductivity data, and the extension to time-lapse SIP data is introduced by Weigand and Kemna (2016), which also examines the influence of RTD discretization on decomposition results. Bérubé et al. (2017) extends the approach of Keery et al. (2012) by developing an adaptive Bayesian inversion scheme that recovers RTD parameters and their posterior distributions for several common relaxation models, including Debye, Warburg, and Cole-Cole models within a unified framework. Lastly, DD is extended to time-domain measurements using a Gauss–Newton scheme in Hase et al. (2023).

Chargeability, indicative of the polarization intensity, and relaxation time, which depends on the critical polarization frequency, are the main DD parameters that can be related to a variety of petrophysical properties. For example, Weller et al. (2010a) and Weller et al. (2010b) relate the normalized chargeability to the specific surface area normalized by the pore volume of sands and sandstones. Additionally, Zisser et al. (2010) and Bairlein et al. (2014) document the effects of temperature, water saturation, and sample preparation on relaxation times and normalized chargeability of sandstones. Moreover, Martin et al. (2021) shows that the relaxation times of pyrite–sand mixtures evolve during desaturation, and Zibulski and Klitzsch (2023) highlights that polarizable grain roughness yields characteristic RTD signatures.

SIP applications that leverage the DD approach in environmental, hydrogeological, and engineering settings are varied. For example, Attwa and Günther (2013) reveals weak correlations between relaxation times and the hydraulic conductivity of an aquifer. Weller et al. (2013) uses DD to estimate water permeability from SIP spectra, and Revil et al. (2014) introduces a Warburg

decomposition that enables inferring pore characteristics from SIP data. Interestingly, Ustra et al. (2012) reports no systematic relationship between RTD parameters and toluene contamination in soils, whereas Flores Orozco et al. (2012) shows increased relaxation times at a hydrocarbon contaminated zone. In civil engineering applications, Khajehnouri et al. (2020a) uses SIP to monitor alkali–silica reaction in concrete samples and shows that chargeability and relaxation times can track its progression. Field applications confirm the versatility of the DD method, as Breede et al. (2012) relates normalized chargeability to clay content in saturated soils, and as Gao et al. (2017) finds that peak relaxation times increase with biochar particle size.

Mineral exploration studies also show that DD is a versatile interpretive tool for petrophysical characterization. Gurin et al. (2013) and Gurin et al. (2015b) use time-domain measurements to estimate the RTD of disseminated ore samples and find that these distributions correlate with mineral composition, grain size, particle content, and pore-solution resistivity. Both laboratory and field measurements confirm the suitability of DD for exploring complex subsurface mineralized targets. For example, Gurin et al. (2015a) applies DD to an Au–Ag deposit and identifies altered zones that contain finely disseminated sulfides. Bérubé et al. (2019) also relates RTD parameters to mineralogical and textural variations in the hydrothermal alteration footprint of the Canadian Malartic Au deposit, and Hase et al. (2023) highlights spatial variations in RTD behavior that align with known geological structures in an ore field.

Despite their widespread use, however, current DD methods have several limitations. Most approaches require a predetermined discretization of relaxation times (e.g., Nordsiek and Weller, 2008), which imposes a prior structure on the RTD. This choice introduces sensitivity to smoothing weights, grid spacing, and initialization (Weigand and Kemna, 2016). A polynomial reparameterization of the RTD can help maintain numerical stability (e.g., Keery et al., 2012), but this approximation adds hyperparameters that strongly influence the RTD. Moreover, conventional DD treats each spectrum independently and does not extract shared structure across samples, thereby preventing analysis of spectral variability at the data set level. Furthermore, existing methods work in real-valued data spaces, even though SIP measurements are complex quantities that obey Kramers–Kronig relationships (Volkman and Klitzsch, 2015). This separation of real and imaginary components, as if they are independent, can limit the accuracy of SIP parameter estimation (e.g., Bérubé et al., 2025).

The aforementioned limitations motivate the development of a complex-valued DD framework that recovers the RTD without predefined discretization or polynomial constraints, quantifies uncertainty, and operates at the data set level. We hypothesize that probabilistic machine learning methods, specifically conditional variational autoencoders (CVAE), offer a natural and flexible means to meet these requirements. Our specific objectives are to (1) develop a CVAE that learns an efficient inverse mapping from SIP data to a continuous RTD, (2) show that the CVAE can

extract interpretable RTD parameters, and (3) demonstrate that latent variables in the CVAE automatically cluster sample populations. The scope of this study is restricted to the analysis of frequency-domain complex resistivity measurements. In the following sections, we start by establishing the continuous RTD formulation, then introduce the machine learning framework. We next describe the laboratory and field data used to develop the approach. The results section reports model selection experiments, curve fitting performance, RTD interpretation, sensitivity and error analyses, and latent space clustering. The discussion section examines the advantages and limitations of machine learning relative to conventional DD methods, and we conclude with a summary of the main findings and an outline of future work.

THEORY

Following Florsch et al. (2014), the modeled isotropic, frequency-dependent, and complex-valued resistivity $\hat{\rho}(\omega)$ stemming from a continuous RTD of elementary Debye models is

$$\hat{\rho}(\omega) = \rho_{\infty} + M \int_0^{\infty} \Gamma(\tau) \lambda(\omega, \tau) d\tau, \quad (1)$$

where ω is the angular frequency in rad/s, τ is the relaxation time in s, ρ_{∞} is the instantaneous resistivity in $\Omega \text{ m}$, and $M = \rho_0 - \rho_{\infty} \geq 0$ is the amplitude of the polarization phenomenon, with ρ_0 denoting the direct current resistivity in $\Omega \text{ m}$. The RTD, denoted by $\Gamma(\tau)$, is normalized such that

$$\int_0^{\infty} \Gamma(\tau) d\tau = 1, \quad (2)$$

and the Debye model is

$$\lambda(\omega, \tau) = \frac{1}{1 + i\omega\tau}, \quad (3)$$

where $i = (-1)^{1/2}$ is the imaginary unit. Using the definition of dimensionless chargeability from Seigel (1959), reading

$$m = \frac{\rho_0 - \rho_{\infty}}{\rho_0}, \quad (4)$$

we rewrite the modeled complex resistivity as

$$\hat{\rho}(\omega) = \rho_0 \left[(1 - m) + m \int_0^{\infty} \Gamma(\tau) \lambda(\omega, \tau) d\tau \right]. \quad (5)$$

It is convenient to express the RTD in logarithmic time coordinates using the change of variable $u = \ln \tau$, in which case the differential reads $d\tau = \tau du$. The integral formulation can therefore be rewritten by defining $\gamma(u) = \tau \Gamma(\tau)$. This quantity represents the chargeability distribution per

logarithmic interval of relaxation time and satisfies

$$\int_{-\infty}^{\infty} \gamma(u) du = 1. \quad (6)$$

Using the change of variable, Equation (5) becomes

$$\hat{\rho}(\omega) = \rho_0 \left[(1 - m) + m \int_{-\infty}^{\infty} \gamma(u) \lambda(\omega, e^u) du \right]. \quad (7)$$

The logarithmic RTD is adopted throughout this study, as it provides uniform resolution over several decades of relaxation times and is standard in the DD literature.

Peak relaxation times, total chargeability, and mean relaxation time are interpretable RTD parameters. Peak relaxation times τ^* are the local maxima of $\gamma(u)$ with $u^* = \ln \tau^*$. Total chargeability truncated over a finite interval $[\tau_1, \tau_2]$, with $u_1 = \ln \tau_1$ and $u_2 = \ln \tau_2$, is

$$m_{[\tau_1, \tau_2]} = m \int_{u_1}^{u_2} \gamma(u) du. \quad (8)$$

The truncated mean relaxation time is defined as the geometric mean in relaxation-time space, $\bar{\tau} = \exp(\bar{u})$, where

$$\bar{u}_{[u_1, u_2]} = \frac{\int_{u_1}^{u_2} u \gamma(u) du}{\int_{u_1}^{u_2} \gamma(u) du}. \quad (9)$$

MACHINE LEARNING

Data preprocessing

Let an SIP data set with J spectra measured at K frequencies be defined as

$$\mathcal{S} = \{(f_k, \rho_{j,k}, \Delta\rho_{j,k}) \mid j = 1, \dots, J, k = 1, \dots, K\}, \quad (10)$$

where f_k denotes the k^{th} measurement frequency in Hz, $\rho_{j,k}$ is the measured complex resistivity of sample j at frequency f_k , and $\Delta\rho_{j,k}$ is its associated complex-valued uncertainty. Complex resistivity stems from multiplying impedance measurements by the geometrical factor G_j , in m, of the electrode configuration, such that

$$\rho_{j,k} = G_j A_{j,k} e^{i\varphi_{j,k}} \quad (11)$$

$$= \rho'_{j,k} + i\rho''_{j,k}, \quad (12)$$

where $A_{j,k}$ is the impedance amplitude in Ω and $\varphi_{j,k}$ is its phase shift in rad, and where $\rho'_{j,k}$ and $\rho''_{j,k}$ denote the real and imaginary parts of resistivity in Ωm , respectively. Each SIP spectrum

is thus represented as a complex-valued vector $\boldsymbol{\rho}_j = [\rho_{j,1}, \dots, \rho_{j,K}] \in \mathbb{C}^K$, an uncertainty vector $\Delta\boldsymbol{\rho}_j = [\Delta\rho_{j,1}, \dots, \Delta\rho_{j,K}] \in \mathbb{C}^K$, and a common frequency vector $\mathbf{f} = [f_1, \dots, f_K] \in \mathbb{R}^K$ for the data set.

Uncertainty propagation follows standard complex error analysis. For each sample j , holding G constant, the total differential of ρ_k with respect to A_k and φ_k yields

$$\Delta\rho_k \simeq G \left(e^{i\varphi_k} \Delta A_k + i A_k e^{i\varphi_k} \Delta\varphi_k \right), \quad (13)$$

leading to the standard deviations of ρ'_k and ρ''_k reading

$$\begin{aligned} \Delta\rho'_k &= G \sqrt{(\cos \varphi_k \Delta A_k)^2 + (A_k \sin \varphi_k \Delta\varphi_k)^2}, \\ \Delta\rho''_k &= G \sqrt{(\sin \varphi_k \Delta A_k)^2 + (A_k \cos \varphi_k \Delta\varphi_k)^2}, \end{aligned} \quad (14)$$

where ΔA_k and $\Delta\varphi_k$ denote the amplitude and phase uncertainties, respectively.

We normalize each spectrum j by its amplitude value at the lowest measurement frequency, $|\rho(f_{\min})|$. This easily reversible normalization reads

$$\tilde{\rho}_k = \frac{\rho_k}{|\rho(f_{\min})|}, \quad \Delta\tilde{\rho}_k = \frac{\Delta\rho_k}{|\rho(f_{\min})|}. \quad (15)$$

Normalization by the low-frequency amplitude is a common strategy for fitting SIP data (e.g., Nordsiek and Weller, 2008; Bérubé et al., 2017), as it constrains the data to a compact region of the complex plane and ensures a stable dynamic range of complex resistivities in the data set. The preprocessed data set is thus

$$\tilde{\mathcal{S}} = \{(f_k, \tilde{\rho}_{j,k}, \Delta\tilde{\rho}_{j,k})\}, \quad (16)$$

where the normalized complex resistivities serve as the input to the machine learning model, the frequencies act as deterministic conditioning variables for the decoder, and the uncertainties are used to weight the optimization objective.

Conditional variational autoencoder

The nonlinear relationship between complex resistivity and a low-dimensional latent representation is modeled using a CVAE (Sohn et al., 2015). In operational form, the CVAE follows the sequence

$$\tilde{\boldsymbol{\rho}} \xrightarrow{\text{encode}} \left(\boldsymbol{\mu}_\phi, \ln \boldsymbol{\sigma}_\phi^2 \right) \xrightarrow{\text{reparameterize}} \mathbf{z} \xrightarrow{\text{decode}|\mathbf{f}} \left(\gamma_\theta, \hat{\boldsymbol{\rho}} \right), \quad (17)$$

where the encoder, with trainable parameters ϕ , maps the input normalized resistivity $\tilde{\boldsymbol{\rho}}$ to the mean $\boldsymbol{\mu}_\phi$ and log-variance $\ln \boldsymbol{\sigma}_\phi^2$ of a diagonal Gaussian approximate posterior. The decoder, with

trainable parameters θ and deterministic conditioning frequencies \mathbf{f} , then maps latent distribution samples \mathbf{z} to the parameters of a logarithmic RTD γ_θ and its associated complex resistivity spectrum $\hat{\boldsymbol{\rho}}$. The CVAE architecture, shown in Figure 1, enforces a generative process in which the latent variables control the complex resistivity through an embedded Debye relaxation model. We implement the CVAE using the PyTorch library (Paszke et al., 2019).

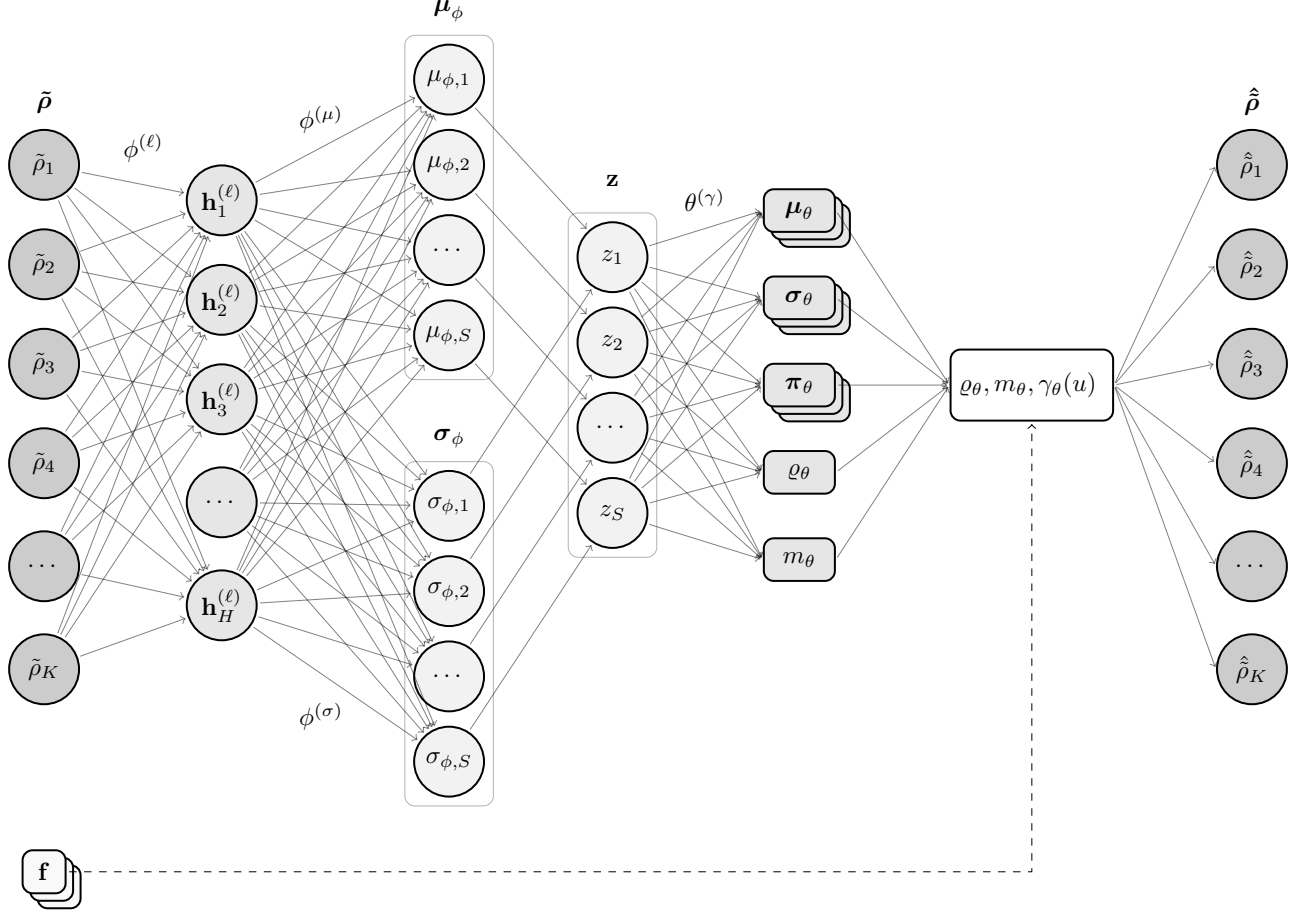


Figure 1: Architecture of the CVAE used for DD. The encoder maps the normalized complex resistivity $\tilde{\boldsymbol{\rho}}$ to the parameters $\boldsymbol{\mu}_\phi$ and $\boldsymbol{\sigma}_\phi$ of a diagonal Gaussian distribution. Latent samples \mathbf{z} are transformed by the decoder, conditioned on the measurement frequencies \mathbf{f} , into the parameters of a Gaussian mixture representation of the logarithmic RTD $\gamma_\theta(u)$. The RTD feeds the forward model in Equation (36) to reconstruct the normalized complex resistivity $\hat{\boldsymbol{\rho}}$.

Encoder

The encoder defines a complex-to-real parametric mapping \mathcal{E}_ϕ from $\tilde{\boldsymbol{\rho}}$ to the parameters of a diagonal Gaussian latent distribution, i.e.,

$$\boldsymbol{\mu}_\phi, \ln \boldsymbol{\sigma}_\phi^2 = \mathcal{E}_\phi(\tilde{\boldsymbol{\rho}}). \quad (18)$$

The mapping \mathcal{E}_ϕ is implemented using a sequence of complex-valued affine transformation layers, each followed by a nonlinear activation function ψ . Starting from the input layer $\mathbf{h}_0 = \tilde{\boldsymbol{\rho}}$, the hidden representations evolve as

$$\mathbf{h}_{\ell+1} = \psi(\mathbf{W}_\ell \mathbf{h}_\ell + \mathbf{b}_\ell), \quad \ell = 0, \dots, L-1, \quad (19)$$

where $\mathbf{W}_\ell \in \mathbb{C}$ and $\mathbf{b}_\ell \in \mathbb{C}$ denote the weight matrices and bias vectors of the ℓ^{th} encoder layer. After L layers, the encoder yields a final hidden representation $\mathbf{h}_L \in \mathbb{C}^H$, where H is the constant width of all hidden layers. We use the complex cardioid nonlinearity of Virtue et al. (2017),

$$\psi(x) = \frac{x(1 + \cos(\arg x))}{2}, \quad x \in \mathbb{C}, \quad (20)$$

which has proven effective for SIP data (Bérubé et al., 2025).

Two parallel complex-valued linear projections map the final hidden representation \mathbf{h}_L to the mean and log-variance of the latent Gaussian distribution through

$$\boldsymbol{\mu}_\phi = \Re(\mathbf{W}_\mu \mathbf{h}_L + \mathbf{b}_\mu) + \Im(\mathbf{W}_\mu \mathbf{h}_L + \mathbf{b}_\mu), \quad (21)$$

and

$$\ln \boldsymbol{\sigma}_\phi^2 = \Re(\mathbf{W}_\sigma \mathbf{h}_L + \mathbf{b}_\sigma) + \Im(\mathbf{W}_\sigma \mathbf{h}_L + \mathbf{b}_\sigma). \quad (22)$$

These quantities define the diagonal Gaussian approximate posterior

$$q_\phi(\mathbf{z} \mid \tilde{\boldsymbol{\rho}}) = \mathcal{N}(\boldsymbol{\mu}_\phi, \text{diag}(\boldsymbol{\sigma}_\phi^2)), \quad \mathbf{z} \in \mathbb{R}^S, \quad (23)$$

where S denotes the latent space dimensionality.

Latent representation

The latent variables are obtained using the reparameterization trick of Kingma and Welling (2014). Given the encoder outputs $\boldsymbol{\mu}_\phi$ and $\ln \boldsymbol{\sigma}_\phi^2$, from which $\boldsymbol{\sigma}_\phi$ is obtained by exponentiation, a stochastic perturbation vector $\boldsymbol{\epsilon} \sim \mathcal{N}(\mathbf{0}, \mathbf{I}_S)$, where \mathbf{I}_S is the identity matrix of size S , is drawn to express the latent variable as

$$\mathbf{z} = \boldsymbol{\mu}_\phi + \boldsymbol{\sigma}_\phi \odot \boldsymbol{\epsilon}, \quad (24)$$

where \odot denotes the Hadamard product. Equation (24) defines a differentiable sampling operation that enables gradient propagation through the stochastic latent space.

Decoder

The decoder maps \mathbf{z} to $\hat{\boldsymbol{\rho}}$, given \mathbf{f} , through a continuous logarithmic RTD parameterized as a Gaussian mixture. This reconstruction yields a generative mapping from the latent representation to modeled SIP spectra. First, the decoder defines a mapping \mathcal{D}_θ from \mathbf{z} and \mathbf{f} to five groups of raw parameters,

$$\tilde{\varrho}_\theta, \tilde{m}_\theta, \tilde{\boldsymbol{\pi}}_\theta, \tilde{\boldsymbol{\mu}}_\theta, \tilde{\boldsymbol{\sigma}}_\theta = \mathcal{D}_\theta(\mathbf{z}, \mathbf{f}), \quad (25)$$

where $\tilde{\varrho}_\theta, \tilde{m}_\theta \in \mathbb{R}$, $\tilde{\boldsymbol{\pi}}_\theta, \tilde{\boldsymbol{\mu}}_\theta, \tilde{\boldsymbol{\sigma}}_\theta \in \mathbb{R}^N$, and N is the number of Gaussian mixture components. The raw parameters are not directly interpretable and must be converted into physical RTD parameters through the following nonlinear functions.

The direct current resistivity ρ_0 is estimated through the scaling factor

$$\varrho_\theta = (1 + 0.1 \tanh(\tilde{\varrho}_\theta)), \quad 0.9 \leq \varrho_\theta \leq 1.1, \quad (26)$$

assuming that $\rho_0 = \varrho_\theta \times |\rho(f_{\min})|$. The bounds of ϱ may be tuned if needed, but we observe that this range fits most SIP spectra. This strategy is also used in Bérubé et al. (2017). Dimensionless chargeability is predicted by the logistic function

$$m_\theta = \frac{1}{1 + \exp(-\tilde{m}_\theta)}, \quad 0 < m_\theta < 1, \quad (27)$$

and the Gaussian mixture weights use the softmax function

$$\pi_{\theta,n} = \frac{\exp(\tilde{\pi}_{\theta,n})}{\sum_l \exp(\tilde{\pi}_{\theta,l})}, \quad n = 1, \dots, N. \quad (28)$$

The decoder places each mixture component at a relaxation time $\tau = e^u$, where u lies in bounds derived from the conditioning frequencies. Knowing that $\omega_k = 2\pi f_k$, the bounds are first determined in common logarithmic space from the inverse angular frequencies ω_k^{-1} , which define the frequency decades spanned by the data. The bounds are then expanded by one decade on each side and converted to natural logarithmic coordinates as

$$u_{\min} = \ln 10 \times \left(\left\lfloor \min_k \log_{10}(\omega_k^{-1}) \right\rfloor - 1 \right), \quad (29)$$

and

$$u_{\max} = \ln 10 \times \left(\left\lceil \max_k \log_{10}(\omega_k^{-1}) \right\rceil + 1 \right), \quad (30)$$

where $\lfloor \cdot \rfloor$ and $\lceil \cdot \rceil$ denote the floor and ceiling operators, respectively.

For numerical evaluation, the decoder represents the RTD as a finite Gaussian mixture in the logarithmic relaxation time coordinate $u = \ln \tau$. Let $u_r \in [u_{\min}, u_{\max}]$ denote a fixed quadrature

grid with spacing Δu . The means of the Gaussian mixture components follow

$$\mu_{\theta,n} = u_{\min} + \frac{u_{\max} - u_{\min}}{2} \left[\tanh(\tilde{\mu}_{\theta,n}) + 1 \right], \quad n = 1, \dots, N, \quad (31)$$

and each Gaussian width is strictly positive through

$$\sigma_{\theta,n} = \exp\left(\frac{1}{2} \tilde{\sigma}_{\theta,n}\right), \quad n = 1, \dots, N. \quad (32)$$

The raw logarithmic RTD thus reads

$$\tilde{\gamma}_{\theta}(u_r) = \sum_{n=1}^N \pi_{\theta,n} \exp\left[-\frac{(u_r - \mu_{\theta,n})^2}{2\sigma_{\theta,n}^2}\right], \quad (33)$$

where the mixture weights satisfy $\pi_{\theta,n} \geq 0$ and $\sum_{n=1}^N \pi_{\theta,n} = 1$. To satisfy the discrete analogue of Equation (6), we normalize the RTD on the quadrature grid as

$$\gamma_{\theta}(u_r) = \frac{\tilde{\gamma}_{\theta}(u_r)}{\sum_r \tilde{\gamma}_{\theta}(u_r) \Delta u}. \quad (34)$$

The continuous RTD integral in Equation (7) is evaluated by numerical quadrature on the logarithmic relaxation time grid, yielding

$$\hat{\rho}(\omega_k) = \rho_0 \left[(1 - m_{\theta}) + m_{\theta} \sum_r \gamma_{\theta}(u_r) \lambda(\omega_k, e^{u_r}) \Delta u \right]. \quad (35)$$

Although the decoder evaluates the RTD on a fixed quadrature grid, the Gaussian mixture formulation defines a continuous RTD that can be evaluated at any $\tau > 0$. Evaluating the RTD on the quadrature grid with $\tau_r = e^{u_r}$ and $m_r = m_{\theta} \gamma_{\theta}(u_r) \Delta u$, however, allows direct comparison with conventional discrete DD. Finally, the decoder output is normalized to match the convention used in Equation (15), i.e.,

$$\hat{\hat{\rho}}(\omega_k) = \varrho_{\theta} \frac{\hat{\rho}(\omega_k)}{\rho_0}. \quad (36)$$

Neural network optimization

We optimize the CVAE parameters by maximizing the evidence lower bound (ELBO), defined for each normalized measured spectrum. The ELBO balances reconstruction fidelity and latent space regularity through

$$\text{ELBO}(\theta, \phi; \tilde{\boldsymbol{\rho}}, \mathbf{f}) = \mathbb{E}_{q_{\phi}(\mathbf{z} | \tilde{\boldsymbol{\rho}})} [\ln p_{\theta}(\tilde{\boldsymbol{\rho}} | \mathbf{z}, \mathbf{f})] - D_{\text{KL}}\left(q_{\phi}(\mathbf{z} | \tilde{\boldsymbol{\rho}}) \parallel p(\mathbf{z})\right), \quad (37)$$

where the expectation term evaluates how likely the measured complex resistivity is under the decoder’s conditional distribution. This term quantifies the agreement between the model and the observations and incorporates the measurement uncertainties. The second term is the Kullback–Leibler divergence (D_{KL}) between the approximate posterior and the prior, which enforces a smooth latent structure by encouraging the encoder’s posterior distribution to remain close to the prior.

Negative log-likelihood

The first term in Equation (37) evaluates the expected log-likelihood of the measured complex resistivity vector $\tilde{\boldsymbol{\rho}}$ under the decoder prediction $\hat{\boldsymbol{\rho}}$. The residual vector is

$$\boldsymbol{\eta} = \tilde{\boldsymbol{\rho}} - \hat{\boldsymbol{\rho}} = (\eta_1, \dots, \eta_K), \quad \eta_k = \eta'_k + i \eta''_k, \quad (38)$$

and a second-order complex Gaussian likelihood is adopted for each frequency component. Conditioned on the latent variable \mathbf{z} and the measurement frequencies \mathbf{f} , the decoder defines the conditional likelihood

$$p_{\theta}(\tilde{\boldsymbol{\rho}} \mid \mathbf{z}, \mathbf{f}) = \prod_{k=1}^K p(\eta_k; v_k, \delta_k), \quad (39)$$

where the variance v_k and pseudo-variance δ_k characterize the second-order statistics of the residual. The corresponding density is derived in Appendix A and reads

$$p(\eta_k; v_k, \delta_k) = \frac{1}{\pi \sqrt{v_k^2 - |\delta_k|^2}} \exp\left(-\frac{v_k |\eta_k|^2 - \Re\{\delta_k^* \eta_k^2\}}{v_k^2 - |\delta_k|^2}\right), \quad (40)$$

which is valid when $v_k > |\delta_k|$. Assuming conditional independence across frequencies, the negative log-likelihood (\mathcal{L}_{NLL}) of the entire complex spectrum is thus

$$\mathcal{L}_{\text{NLL}} = \sum_{k=1}^K \left[\frac{v_k |\eta_k|^2 - \Re\{\delta_k^* \eta_k^2\}}{v_k^2 - |\delta_k|^2} + \frac{1}{2} \ln(v_k^2 - |\delta_k|^2) + \ln(\pi) \right]. \quad (41)$$

The term $v_k^2 - |\delta_k|^2$ in Equation (41) may approach zero when the empirical variance and pseudo-variance are nearly degenerate, which leads to numerical instabilities in the evaluation of \mathcal{L}_{NLL} . To avoid this situation, we impose a minimum threshold and replace it by $\max(v_k^2 - |\delta_k|^2, 10^{-12})$. We observe that 10^{-12} is the smallest threshold that prevents divergence of \mathcal{L}_{NLL} and ensures numerically stable training.

When normalized uncertainty estimates $\Delta \tilde{\rho}'_k$ and $\Delta \tilde{\rho}''_k$ are available at each frequency, the variance and pseudo-variance at frequency f_k are

$$v_k = (\Delta \tilde{\rho}'_k)^2 + (\Delta \tilde{\rho}''_k)^2, \quad \delta_k = (\Delta \tilde{\rho}'_k)^2 - (\Delta \tilde{\rho}''_k)^2 + 2i \text{Cov}(\Delta \tilde{\rho}'_k, \Delta \tilde{\rho}''_k), \quad (42)$$

respectively, where $\text{Cov}(\Delta\tilde{\rho}'_k, \Delta\tilde{\rho}''_k)$ denotes the covariance between the real and imaginary uncertainty components. If uncertainties are unknown, v_k and δ_k can be estimated by computing expectations over the residuals at each iteration.

Kullback–Leibler divergence

The second ELBO term regularizes the latent space. The latent prior is the standard normal distribution and the encoder defines the diagonal Gaussian posterior in Equation (23). For each SIP spectrum, the D_{KL} between the approximate posterior and the prior admits the closed-form expression (Kingma and Welling, 2014)

$$D_{\text{KL}}(q_\phi(\mathbf{z} | \tilde{\boldsymbol{\rho}}) \parallel p(\mathbf{z})) = \frac{1}{2} \sum_{s=1}^S (\mu_{\phi,s}^2 + \sigma_{\phi,s}^2 - 1 - \ln \sigma_{\phi,s}^2). \quad (43)$$

This term penalizes departures of the posterior distribution from the isotropic unit-Gaussian prior and therefore constrains the geometry of the latent space.

Training procedure

The total loss function is the negative ELBO,

$$\mathcal{L}(\theta, \phi; \tilde{\boldsymbol{\rho}}, \mathbf{f}) = -\text{ELBO}(\theta, \phi; \tilde{\boldsymbol{\rho}}, \mathbf{f}) \quad (44)$$

$$= \mathcal{L}_{\text{NLL}} + D_{\text{KL}}, \quad (45)$$

which is minimized by tuning the CVAE parameters. Gradient-based optimization is performed with respect to the complex conjugate of the neural network weights, i.e., $\partial\mathcal{L}/\partial\mathbf{W}^*$. The loss \mathcal{L} is real-valued, and gradients with respect to complex parameters are computed using Wirtinger calculus,

$$\frac{\partial\mathcal{L}}{\partial\mathbf{W}^*} = \frac{1}{2} \left(\frac{\partial\mathcal{L}}{\partial\mathbf{W}'} + i \frac{\partial\mathcal{L}}{\partial\mathbf{W}''} \right), \quad (46)$$

with an analogous expression for the bias parameters. We use the PyTorch implementation of the Adam optimizer (Kingma and Ba, 2015), with an initial learning rate of 10^{-3} , to minimize \mathcal{L} . Training is stopped once the loss shows less than a 1% relative improvement between two consecutive windows of 1000 iterations.

Error metrics

Let $\mathbf{x} \in \mathbb{R}^{J \times K}$ denote a reference normalized SIP attribute (e.g., magnitude $|\tilde{\rho}|$, real part $\tilde{\rho}'$, or imaginary part $\tilde{\rho}''$), and let $\hat{\mathbf{x}}$ be its prediction. We define the elementwise normalized absolute error as

$$\varepsilon(\mathbf{x}) = \left| \frac{\hat{\mathbf{x}} - \mathbf{x}}{\max(\mathbf{x}) - \min(\mathbf{x})} \right|, \quad (47)$$

where the max and min operators are taken over all samples and frequencies, so that the denominator is based on the dynamic range of the attribute. This range typically lies in $[0, 1]$ due to the data normalization strategy in Equation (15).

The normalized mean absolute error (NMAE), expressed in percent, is thus

$$\text{NMAE} = 100 \langle \varepsilon(\mathbf{x}) \rangle, \quad (48)$$

where $\langle \cdot \rangle$ denotes averaging. Depending on the chosen averaging domain, Equation (48) yields (i) a global NMAE when the average is taken over both samples and frequencies, (ii) a frequency-dependent NMAE when the average is taken over samples, and (iii) a sample-dependent NMAE when the average is taken over frequencies.

DATA SET

The data set consists of laboratory and field SIP measurements from unconsolidated and consolidated materials. All SIP data sets are measured using the same SIP-Fuchs-III instrument (Radic Research, Germany) at 19 logarithmically spaced frequencies in the 90 mHz to 20 kHz range. Each spectrum in the data set is measured twice under identical conditions; the mean of the two measurements is the final value, and their standard deviation is the measurement uncertainty. Table 1 provides an overview of the SIP data included in this study, together with their sample counts and references.

Table 1: Summary of the selected SIP data sets used in this study.

Data source	Reference	Number of samples
Pyrite–sand mixtures	This study	30
Graphite–sand mixtures	Benzetta (2024)	25
Stainless steel spheres	This study	11
Stainless steel cylinders	This study	6
Canadian Malartic rock cores	Bérubé et al. (2019)	12
Highland Valley rock cores	Grenon (2018)	5
Canadian Malartic field data	Bérubé et al. (2019)	26
Concrete samples	Khajehnouri et al. (2020b)	25
Total		140

Unconsolidated materials

Mixtures of polarizable grains embedded in a nonconductive clean sand matrix are prepared to investigate the dependence of SIP on conductive phase properties and volumetric content. All mixtures use the same feldspar sand with diameter (d) characteristics reported in Table 2. The sand is air-dried, poured into the sample holders without mechanical compaction, and saturated by slow filling with a KCl solution.

Table 2: Grain-size descriptors of the feldspar sand obtained from sieve analysis. d_{10} , d_{30} , d_{50} , and d_{60} are the particle diameters for which 10 %, 30 %, 50 %, and 60 % of the sample mass pass the sieve, respectively. $C_u = d_{60}/d_{10}$ is the coefficient of uniformity. $C_c = d_{30}^2/(d_{10}d_{60})$ is the coefficient of curvature. The $C_u < 6$ and low C_c values show that the sand has a narrow grain size distribution (Holtz and Kovacs, 1981).

Grain size parameter	Value
d_{10} (mm)	0.104
d_{30} (mm)	0.173
d_{50} (mm)	0.227
d_{60} (mm)	0.254
C_u	2.45
C_c	1.14

Pyrite–sand mixtures

This sample series consists of 30 mixtures of feldspar sand and pyrite grains. Three pyrite size classes are considered: (i) ≤ 0.5 mm, (ii) 0.5–1 mm, and (iii) 1–3 mm. For each class, ten mixtures are prepared with pyrite volume fractions ranging from 1 % to 10 %. The mixtures consist of a fixed sand mass of 59.6 g and a variable pyrite mass calculated from densities of 2.65 and 5.0 g cm⁻³,

respectively. SIP measurements are performed in a cylindrical insulating cell of 2.6 cm internal diameter and 7 cm length, equipped with stainless steel disk electrodes for current injection and nonpolarizable electrodes for voltage measurement. The KCl solution used for saturation has a conductivity of $160 \mu\text{S cm}^{-1}$ at 21 °C. The lack of intrinsic sample holder polarization is validated through measurements on the KCl solution only.

Graphite-sand mixtures

This series of samples consists of 25 feldspar sand and graphite mixtures, prepared to investigate the SIP response associated with semimetallic particles (Benzetta, 2024). The graphite grains have a mean diameter of 44 μm . Each mixture is obtained by thoroughly mixing the sand and graphite to reach target graphite volume fractions between 0.2% and 5.0%, assuming the density of graphite is 2.26 g cm^{-3} , followed by slow filling with a KCl electrolyte of conductivity $37 \mu\text{S cm}^{-1}$ at 21 °C. The same sample holder and measurement protocol as for the pyrite mixtures are used.

Stainless steel inclusions

We include 17 SIP measurements performed on grade 304 stainless steel spheres and cylinders embedded in saturated feldspar sand. The KCl solution used for saturation has a conductivity of $333 \mu\text{S cm}^{-1}$ at 21 °C. These measurements use a sand box that replicates a miniature Schlumberger array rather than the cylindrical cell employed for the pyrite and graphite mixtures. The setup uses copper needles as current electrodes and Ag-AgCl electrodes as potential electrodes, with a 124 mm current-electrode spacing and a 20 mm potential-electrode spacing. For each measurement, a single stainless steel sphere or cylinder is placed at the center of the array to allow for controlled variations in polarizable grain size. The cylinders are placed perpendicular to the injected current direction. The tested diameters are 2, 2.5, 3, 3.5, 4, 4.5, 5, 5.5, 6, 7, and 8 mm for the spheres and 2, 2.5, 3, 4, 5, and 6 mm for the cylinders. These samples create a simple reference system to study the effect of metallic grain size on SIP signatures in the absence of mineralogical or textural complexity.

Consolidated materials

Mineralized rock samples

These laboratory measurements include 12 complex resistivity spectra of core samples from the hydrothermal footprint of the sulfide-associated Canadian Malartic Au deposit, as well as five spectra from the Highland Valley porphyry Cu deposit. The mineralogy, texture, and complex

resistivity spectra of the Canadian Malartic samples are analyzed in Bérubé et al. (2019). The SIP signatures of the Highland Valley samples are described in Grenon (2018). In both cases, the rock samples have been coated with paraffin wax, leaving both end faces exposed for electrical contact, and saturated for 48 hours in a common electrolyte to prevent salinity-related variations in SIP response. A dedicated sample holder maintains constant saturation and minimizes contact impedance using Ag–AgCl potential electrodes and copper current electrodes. Each spectrum is measured twice with three acquisition cycles per frequency to estimate amplitude and phase uncertainties. Further details on the experimental procedure is available in Bérubé et al. (2019).

Outcrop measurements

The field component of our data set consists of SIP measurements at 26 stations along a north–south profile, using a Wenner array with a one meter electrode spacing, on the Bravo Zone outcrop of the Canadian Malartic Au deposit. The outcrop exposes steeply dipping sedimentary units cut by felsic to intermediate intrusions, with localized gold mineralization and hydrothermal alteration. Additional details on the outcrop geology and measurement protocol are available in Bérubé et al. (2019).

Concrete samples

We include 25 SIP measurements of concrete samples to increase the diversity of materials represented in the data set. Of the 25 samples, 12 are reactive concrete affected by the alkali–silica reaction and 13 are nonreactive. The samples consist of cylindrical concrete specimens with a diameter of 76 mm and a length of 190 mm, prepared using a general-purpose cement and identical aggregate size distributions. Reactive samples contain coarse silica-rich aggregates from Placitas (New Mexico, USA), whereas nonreactive samples use limestone and dolomite aggregates from the Saint-Dominique quarry (Quebec, CA). All concrete specimens are cast simultaneously and removed from their molds after curing for 24 h. The preparation of the concrete samples and the associated SIP measurement protocol are described in Khajehnouri et al. (2020b), which presents time-lapse SIP measurements acquired during accelerated alkali–silica reaction tests on reactive and nonreactive concrete mixtures. The accuracy of the SIP measurement system used for the concrete samples is valid over the 1.43 mHz to 20 kHz frequency range (Khajehnouri et al., 2019).

RESULTS

The results are structured in three themes. We start by selecting an efficient CVAE architecture, then apply the machine learning approach to laboratory and field SIP measurements, interpret the

inferred RTD parameters, and finally we analyze the model sensitivity, its error patterns and the geometry of its latent space.

Model selection

We evaluate the NMAE between the measured and modeled SIP spectra over a range of CVAE configurations to select an efficient DD model. This section presents experimental results for the latent space, decoder, and encoder architectures selection, as well as the training behavior of the final model configuration.

Latent space and decoder

Figure 2 summarizes the NMAE between measured and modeled data using varying latent space dimensionality S and number of Gaussian mixture components N . To ensure that the latent space constitutes the effective bottleneck of the model, we start by using an intentionally wide encoder with 32 neurons and a large Gaussian mixture expansion of 32 components in the decoder. After identifying the ideal value for S (Figure 2a), we vary N in the decoder (Figure 2b). All models are trained with identical settings, and we average the results across three experiment repetitions.

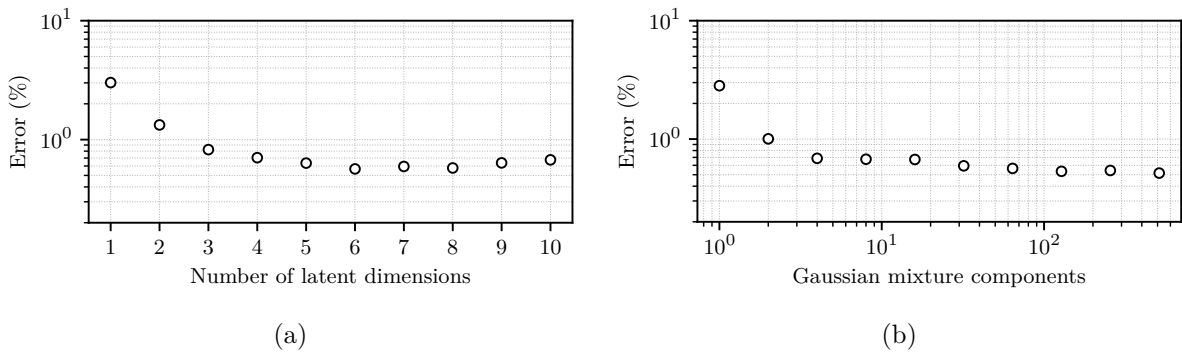


Figure 2: Model selection experiment with respect to the number of latent dimensions (a) and Gaussian mixture components (b) used by the decoder. Markers correspond to the NMAE averaged over the real and imaginary parts and three experiment repetitions. Error bars corresponding to the standard deviation of the results across repetitions are smaller than the markers.

Figure 2a shows that the reconstruction accuracy improves rapidly as the latent dimension increases from $S = 1$ to $S = 3$. The NMAE on ρ' decreases from 2.85% at $S = 1$ to 1.27% at $S = 2$ and reaches 0.80% at $S = 3$, with similar reductions in the errors on ρ'' . Increasing the dimension to $S = 4$ yields only a modest improvement, reducing the NMAE to 0.71% for ρ' and 0.70% for ρ'' . The lowest errors are obtained for $S = 5$ and $S = 6$, where the NMAE stabilizes

near 0.63 % and 0.60 % for ρ' , and 0.64 % and 0.54 % for ρ'' , respectively. Beyond six dimensions, the NMAE no longer improves and becomes increasingly unstable, with growing variability across repetitions and noticeable degradation for $S \geq 9$. We therefore adopt $S = 6$, which captures the nonlinear variability of the SIP spectra without introducing excess capacity, as the optimal latent dimension for the remainder of this study.

Figure 2b reveals that errors decrease rapidly as the number of Gaussian mixture components increases from 1 to 128. Over this range, the NMAE on ρ' decreases from 2.56 % at $N = 1$ to 0.57 % at $N = 128$, while the NMAE on ρ'' decreases from 3.08 % to 0.50 %. Increasing the mixture dimension beyond $N = 128$ yields only minor improvements. The NMAE for $N = 256$ and $N = 512$ remain in the ranges 0.56–0.59 % for ρ' and 0.47–0.49 % for ρ'' . These results indicate that selecting $N \geq 100$ provides sufficient resolution for the RTD, and that larger numbers of mixture components introduce redundancy without improving curve fitting quality. We therefore select $N = 128$ for all subsequent experiments.

Encoder architecture

Figure 3 summarizes the results of the grid search performed to identify the optimal encoder architecture by varying both the number of hidden layers and the width of each layer. The reported values correspond to the average NMAE of three experiment repetitions, and the uncertainties are the standard deviations across the repetitions.

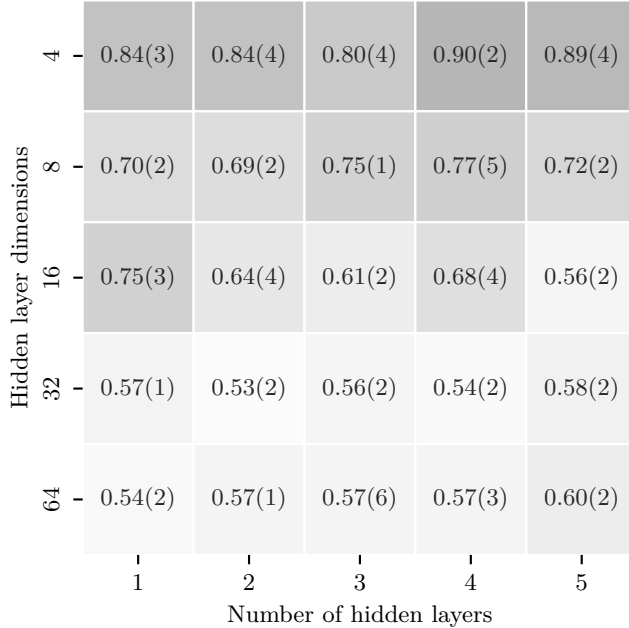


Figure 3: Heatmap of the modeled complex resistivity NMAE as a function of the number of hidden layers and the hidden layer dimension in the CVAE encoder. Each cell reports the mean and standard deviation of three experiment repetitions. Darker cells correspond to higher errors. The optimal model choice has two layers of 32 units.

The grid search shows that the encoder benefits primarily from increased layer width, with depth playing a secondary role. For example, with a single hidden layer, the NMAE decreases from $0.84 \pm 0.03\%$ at dimension 4 to $0.54 \pm 0.02\%$ at dimension 64. Two-layer encoders follow the same trend and achieve the best overall performance at a width of 32, yielding the lowest reconstruction error of $0.53 \pm 0.02\%$. Increasing the width beyond 32 does not improve accuracy for the two-layer case and slightly degrades performance to $0.57 \pm 0.01\%$ at dimension 64. Increasing depth beyond two layers does not provide systematic gains at fixed width. Three- to five-layer networks remain close to the best model only for the widest settings, with errors between 0.54 and 0.60% for widths 32–64, while deeper architectures yield larger errors for narrow widths. We therefore select an encoder with two hidden layers of dimension 32 for all subsequent experiments.

Learning curves

The learning curves shown in Figure 4 indicate that optimization of the CVAE is a stable process. The negative log-likelihood decreases substantially during training, from an initial value of 2.43×10^1 to 4.93×10^{-3} , corresponding to a reduction factor of 4.93×10^3 over 33,034 steps. This decrease reflects rapid convergence toward accurate reconstructions. Although the log-log scale used in Figure 4 amplifies small variations, the standard deviation of 4.19×10^{-3} over the last 1000 iterations confirms that the optimization stabilizes with minor oscillations before training is

stopped.

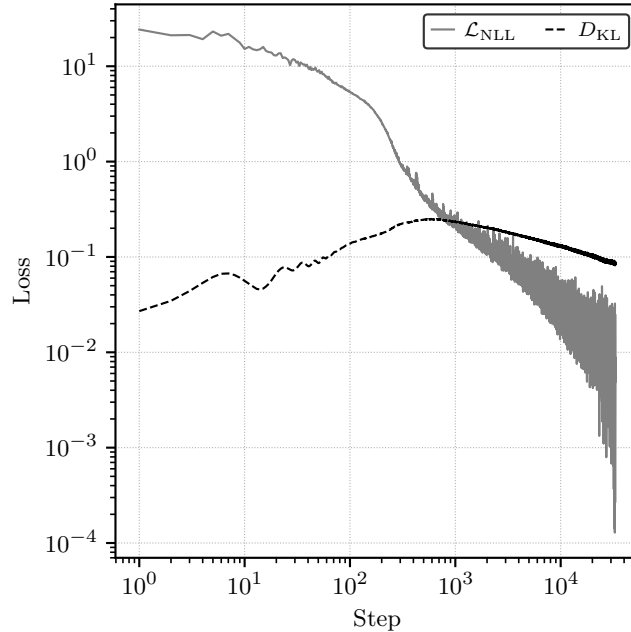


Figure 4: Learning curves of the selected CVAE. The plot shows the evolution of the negative log-likelihood term (\mathcal{L}_{NLL}) and the Kullback–Leibler divergence (D_{KL}) as a function of the optimization step. Training is stopped once the total loss ($\mathcal{L}_{\text{NLL}} + D_{\text{KL}}$) does not improve by more than 1% in the last 1000 steps.

The Kullback–Leibler divergence evolves consistently with its intended regularization goal (Figure 4). It begins at 8.79×10^{-2} and ends at 9.46×10^{-2} , a modest growth factor of 1.08. Its standard deviation in the last 10% of iterations is small (1.99×10^{-3}), indicating that the posterior distribution does not collapse. The learning curves show that during the first ~ 500 steps the CVAE prioritizes accurate SIP data reconstruction. After this initial phase, the optimization begins to regularize the latent space while continuing to reduce the data misfit at a slower rate.

Model applications

We apply the selected CVAE model to several tasks to demonstrate its accuracy, interpretability, and practical value for SIP data analysis. These tasks include curve fitting, estimation and interpretation of the RTD and its integrating parameters, and artificial generation of realistic SIP responses. These examples validate the machine learning approach on actual data and illustrate how the learned latent representation supports both quantitative and qualitative geophysical interpretation.

Curve fitting

The four curve fitting examples in Figure 5 show that the CVAE reproduces a wide range of SIP responses with low reconstruction error. Across the selected samples, the NMAE for ρ' remains below 1.6 % (between 0.39 % and 1.51 %), and the NMAE for ρ'' lies between 0.22 % and 1.20 %. In all cases, the predicted mean curves closely follow the observed frequency dependence over the entire range.

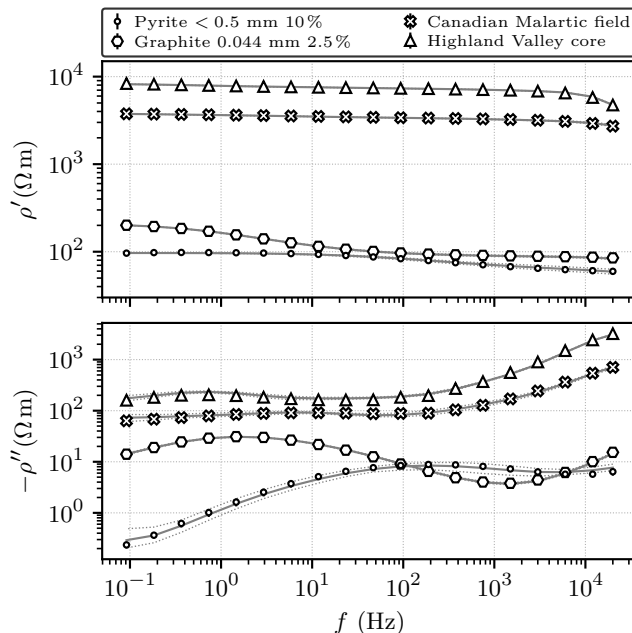


Figure 5: Examples of CVAE reconstructions for four SIP spectra drawn from laboratory and field measurements. For each sample, the observed real and imaginary parts are plotted with their measurement error bars, and the mean CVAE prediction (solid line) is shown together with its 95 % posterior confidence interval (dotted lines). The examples span a wide range of spectral responses, including a pyrite–sand mixture, a graphite–sand mixture, and heterogeneous rock core and field measurements.

The CVAE produces accurate fits while expressing sample-dependent posterior variability. The laboratory measurements exhibit relatively narrow error bars (smaller than the markers in Figure 5), with average widths ranging from 0.50 to 1.26 Ωm for ρ' and from 0.08 to 0.46 Ωm for ρ'' . Field and core measurements show larger uncertainty, with ρ' and ρ'' error bars reaching average values of 0.81 to 6.76 Ωm , respectively. The posterior standard deviations predicted by the CVAE span several orders of magnitude depending on the sample, with mean values between 0.67 and 25.9 Ωm for ρ' , and between 0.21 and 11.4 Ωm for ρ'' . These model-derived uncertainties are consistently wider than the experimental error bars, yet the predicted confidence intervals remain visually aligned with the data.

Relaxation time distribution

Figure 6 summarizes the posterior distribution of the RTD for a representative SIP spectrum by jointly displaying its discrete and continuous representations. The RTD is that of the 2.5% graphite–sand mixture for which the spectrum is illustrated in Figure 5. The carpet plot shows an ensemble of 100 posterior RTD realizations evaluated on the fixed quadrature grid, where each horizontal row represents one posterior sample and the grayscale intensity denotes the chargeability assigned to each relaxation time bin. This visualization highlights both the variability of the inferred RTD across the posterior distribution and the persistence of the main relaxation time peaks. Superimposed on the carpet plot, the black solid curve shows the median continuous RTD reconstructed from the Gaussian mixture representation, and the dotted curves indicate its 95% confidence interval. The combined representation allows comparison between the discrete chargeability bins produced by the quadrature integration and the continuous RTD density inferred by the probabilistic model.

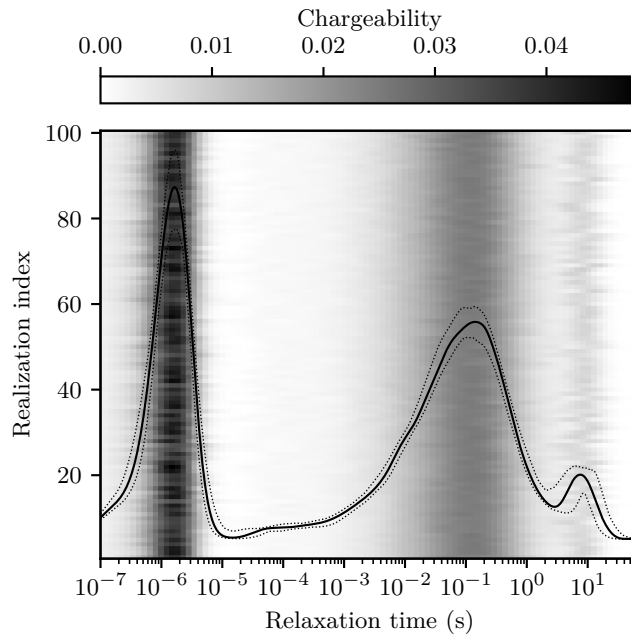


Figure 6: Posterior RTD of the 2.5% graphite–sand mixture. The carpet plot shows 100 posterior RTD realizations evaluated on the quadrature grid, where each row corresponds to one realization and grayscale intensity reflects chargeability. The black solid curve is the median continuous RTD from the Gaussian mixture model, and the dotted curves show its 95% confidence interval.

The posterior RTD in Figure 6 exhibits a stable and well-resolved multimodal structure. Across the 100 posterior realizations, the total chargeability inferred from the quadrature representation is 0.95, on average, with a standard deviation of 0.01. The continuous RTD reveals two dominant modes that are consistently recovered across the posterior distribution. The first mode peaks at a short relaxation time of $\tau^* \approx 1.6 \times 10^{-6}$ s. By integrating the peak above its half-height,

we find that it contributes approximately 27% of the total chargeability, despite exhibiting the highest peak density in the RTD. This is due to its relatively narrow half-height width, which indicates a well-localized relaxation process. The first mode corresponds to the so-called high-frequency response typical in SIP measurements, which can be attributed to a dielectric response or capacitive coupling (e.g., Revil, 2013; Florsch et al., 2014). In contrast, the second mode peaks at a longer relaxation time of $\tau^* \approx 1.4 \times 10^{-1}$ s and accounts for a larger fraction of the total chargeability, about 40%, while displaying a lower peak density but a substantially broader width. A third, minor peak is observed at $\tau^* \approx 8$ s, which is near the upper bound for τ .

Analyzing the RTD of all 140 samples in the data set shows that a valley at $\tau = 100 \mu\text{s}$ is systematically present between the high-frequency and low-frequency polarization responses. We therefore analyze the low-frequency response by truncating the integrating parameters in the range between $100 \mu\text{s}$ and 10 s. In this range, distinct RTD signatures emerge for each material class, and within-series variability remains lower than between-series variability, as evidenced in Figure 7.

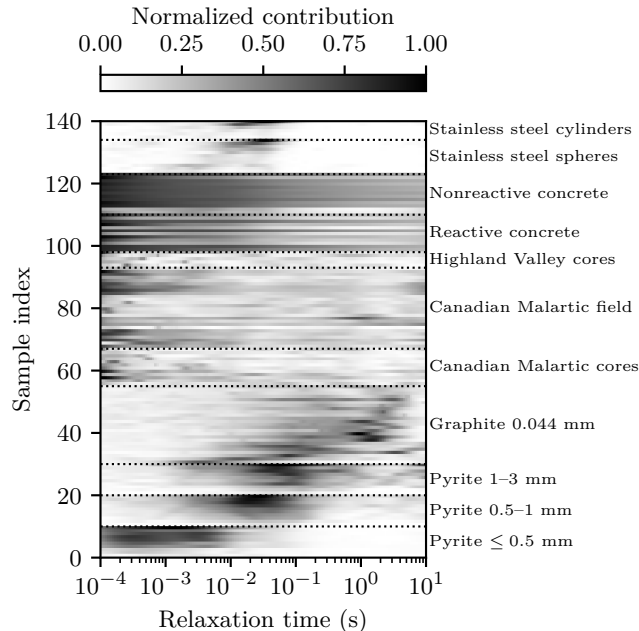


Figure 7: Block-normalized heatmap of the posterior RTD inferred by the CVAE. Each row corresponds to one SIP spectrum in the data set, and the grayscale represents the contribution of the Gaussian mixture components to the RTD as a function of relaxation time. Contributions are computed from the median posterior parameters and normalized within each sample series to emphasize relative RTD structure rather than absolute chargeability. Horizontal dotted lines delineate sample groups.

Integrating parameters

Figure 8 summarizes the joint distribution of truncated mean relaxation time $\bar{\tau}_{[10^{-4}, 10^1]}$ and total chargeability $m_{[10^{-4}, 10^1]}$ for all material groups in the data set, and Table 3 reports the correspond-

ing group-level statistics. Together, these representations highlight systematic contrasts between granular mixtures, natural rock samples, and cementitious materials. The posterior uncertainty on $\bar{\tau}$ and m remains small relative to the spread between material groups, which confirms that the CVAE provides well-resolved integrating parameters suitable for comparisons.

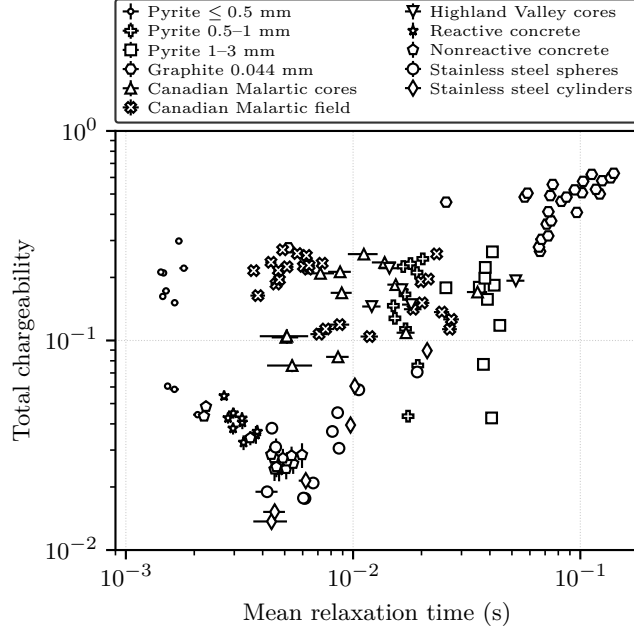


Figure 8: Total chargeability $m_{[10^{-4}, 10^1]}$ as a function of mean relaxation time $\bar{\tau}_{[10^{-4}, 10^1]}$ for all material groups in the data set. Each marker corresponds to a single SIP spectrum, with symbols distinguishing the different sample groups. The distribution of points highlights systematic contrasts between pyrite and graphite mixtures, natural rock samples, concrete, and stainless steel inclusions in terms of both polarization strength and characteristic timescale.

Table 3: Group-level means and standard deviations (s.d.) of the truncated mean relaxation time $\bar{\tau}_{[10^{-4}, 10^1]}$ and total chargeability $m_{[10^{-4}, 10^1]}$.

Sample group	$\bar{\tau}$ mean (s)	$\bar{\tau}$ s.d. (s)	m mean	m s.d.
Pyrite ≤ 0.5 mm	1.62×10^{-3}	1.98×10^{-4}	0.159	0.083
Pyrite 0.5–1 mm	1.75×10^{-2}	1.69×10^{-3}	0.159	0.069
Pyrite 1–3 mm	3.82×10^{-2}	5.04×10^{-3}	0.162	0.067
Graphite 0.044 mm	8.41×10^{-2}	3.19×10^{-2}	0.459	0.111
Canadian Malartic cores	1.18×10^{-2}	8.41×10^{-3}	0.160	0.063
Canadian Malartic field	1.12×10^{-2}	8.18×10^{-3}	0.188	0.054
Highland Valley cores	2.26×10^{-2}	1.66×10^{-2}	0.177	0.032
Reactive concrete	3.55×10^{-3}	7.11×10^{-4}	0.038	0.008
Nonreactive concrete	4.45×10^{-3}	1.15×10^{-3}	0.030	0.008
Stainless steel spheres	7.92×10^{-3}	4.24×10^{-3}	0.035	0.017
Stainless steel cylinders	9.37×10^{-3}	6.31×10^{-3}	0.040	0.030

The three pyrite grain-size series form a coherent trend characterized by nearly constant chargeability and progressively increasing relaxation times. Across all grain sizes, the mean total chargeability remains close to ≈ 0.16 , whereas the mean relaxation time increases from 1.6×10^{-3} s for the finest grains to 3.8×10^{-2} s for the coarsest fraction. These results show that grain size primarily controls the polarization timescale, whereas the polarization strength is mostly insensitive to grain size over the investigated range.

Graphite mixtures occupy a distinct region of the $(\bar{\tau}, m)$ space in Figure 8, with both substantially higher chargeability and longer relaxation times than any of the pyrite series. The mean total chargeability for graphite is ≈ 0.46 , nearly three times that of pyrite, and the mean relaxation time is on the order of 10^{-1} s. In contrast to pyrite, graphite exhibits a much broader distribution of relaxation times, reflected by a large dispersion in $\bar{\tau}$ and m . This combination indicates strong but heterogeneous polarization behavior, as also described in Figure 9.

Natural rock samples from the Canadian Malartic and Highland Valley deposits cluster at intermediate relaxation times, typically around 10^{-2} s, with moderate chargeability values between 0.16 and 0.19. Core and field measurements from the Canadian Malartic deposit largely overlap in the $(\bar{\tau}, m)$ space, despite their different acquisition conditions, which suggests that the integrating parameters mostly capture material properties rather than measurement-specific effects. The relatively large variability in $\bar{\tau}$ within these groups reflects the heterogeneity of natural rocks.

Concrete samples form a separate cluster characterized by short relaxation times and low chargeability. Reactive and nonreactive concretes both exhibit $\bar{\tau}$ values of a few 10^{-3} s and $m < 0.04$, with reactive concrete showing slightly higher chargeability, consistently with Khajehnouri et al. (2020a). Lastly, stainless steel inclusions in sand occupy an intermediate regime, with $\bar{\tau}$ comparable to those of pyrite and graphite but much lower m because only one inclusion is present per sample.

Total chargeability

Figure 9 shows the relationship between truncated total chargeability normalized by the direct current resistivity, $m_{[10^{-4}, 10^1]}/\rho_0$, and volumetric fraction for the three pyrite grain-size series and the graphite-sand mixtures. For all materials, the normalized chargeability increases linearly with volumetric fraction, which indicates that the integrating parameter extracted from the RTD scales proportionally with the abundance of polarizable grains. The strength of this relationship is high for all pyrite mixtures, with coefficients of determination between 0.95 and 0.98 and Pearson correlation coefficients exceeding 0.96. The regression residuals remain small relative to the signal amplitude, with root-mean-square errors below $2 \mu\text{S}/\text{m}$.

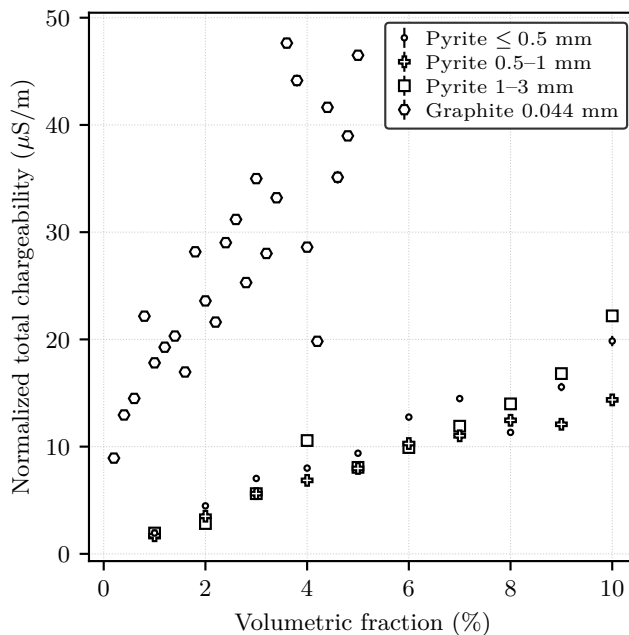


Figure 9: Truncated normalized total chargeability $m_{[10^{-4}, 10^1]}/\rho_0$ as a function of volumetric fraction for pyrite and graphite sand mixtures. Markers denote different grain-size series, and error bars represent posterior standard deviations. The data reveal an approximately linear increase of normalized chargeability with polarizable mineral content, with a markedly higher sensitivity for graphite compared with pyrite.

The three pyrite grain-size series exhibit similar slopes, ranging from 1.50 to 1.86 $\mu\text{S}/\text{m}$ per volumetric percent, and small intercepts that remain close to zero within uncertainty. The finest pyrite grains (≤ 0.5 mm) yield a slope of 1.86 ± 0.13 $\mu\text{S}/\text{m}$ per %, while the 0.5–1 mm series exhibits a slightly smaller slope of 1.50 ± 0.07 $\mu\text{S}/\text{m}$ per %. The coarsest grains (1–3 mm) produce a slope of 1.83 ± 0.15 $\mu\text{S}/\text{m}$ per %. A likelihood-ratio test provides moderate evidence against the null hypothesis of a single common slope across the three pyrite series ($p = 0.027$).

The graphite–sand mixtures follow a linear trend with a substantially larger slope of 4.54 ± 0.87 $\mu\text{S}/\text{m}$ per %, more than twice that of any pyrite series, and a large positive intercept of 14.1 ± 2.1 $\mu\text{S}/\text{m}$. The correlation is weaker (determination coefficient of 0.54 and Pearson coefficient of 0.82), and the regression residuals are larger (RMSE = 6.49 $\mu\text{S}/\text{m}$), reflecting the broader variability of the graphite responses (Figure 9). These results highlight the higher intrinsic polarizability of graphite powder relative to pyrite grains and indicate that, while total chargeability still scales with volumetric fraction, graphite mixtures have greater RTD variability.

Mean relaxation time

Figure 10 illustrates the relationship between the truncated mean relaxation time $\bar{\tau}_{[10^{-4}, 10^1]}$ and inclusion diameter for stainless steel spheres and cylinders embedded in feldspar sand. For both

geometries, $\bar{\tau}$ increases systematically with inclusion size, which indicates that the dominant polarization timescale recovered by the CVAE is controlled by the characteristic dimension of the polarizable inclusions. The data are well described by a power-law relationship of the form $\bar{\tau} = \beta d^\alpha$, as evidenced by strong correlations in log–log space for both series.

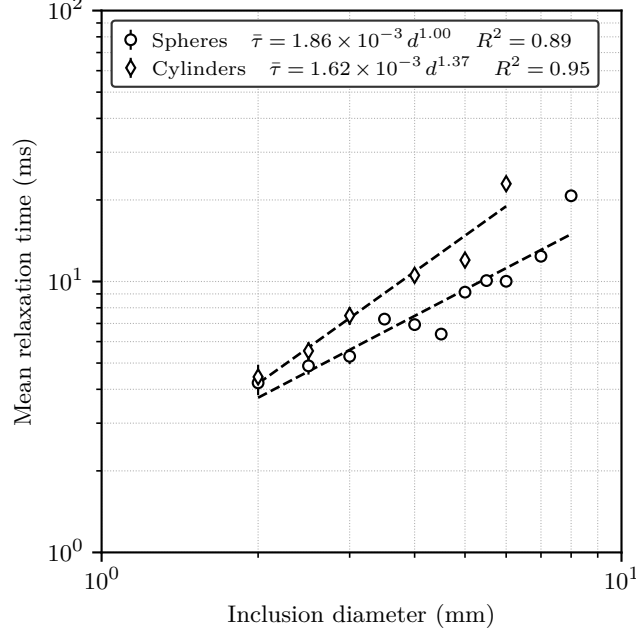


Figure 10: Truncated mean relaxation time $\bar{\tau}_{[10^{-4}, 10^1]}$, in ms, as a function of inclusion diameter (d), in mm, for stainless steel spheres and cylinders in feldspar sand. Error bars represent posterior uncertainty from the probabilistic DD. The data show a systematic increase of $\bar{\tau}$ with inclusion size for both geometries.

For spherical inclusions, the fitted scaling exponent is $\alpha = 1.00 \pm 0.12$, with a coefficient of determination of 0.89 and a root-mean-square error of 1.9×10^{-3} s. The exponent indicates an approximately linear scaling between the mean relaxation time and sphere diameter over the investigated range from 2 to 8 mm. The corresponding prefactor is $\beta = 1.86 \times 10^{-3}$ s mm $^{-\alpha}$, which yields $\bar{\tau}$ spanning from approximately 3.7×10^{-3} s to 1.5×10^{-2} s, consistent with the observations in Figure 10.

Cylindrical inclusions exhibit a steeper dependence, with a fitted exponent of $\alpha = 1.37 \pm 0.15$ and a higher determination coefficient of 0.95. The prefactor for cylinders, $\beta = 1.62 \times 10^{-3}$ s mm $^{-\alpha}$, is of the same order of magnitude as that obtained for spheres, and the resulting relaxation times span a comparable range. A direct comparison of the fitted exponents yields $\Delta\alpha = -0.37 \pm 0.19$. Although the cylindrical exponent is larger, the difference remains close to the limit of statistical significance given the limited number of samples. These results show that the CVAE-derived mean relaxation time exhibits a clear size dependence, consistent with theoretical models of interfacial polarization (e.g., Misra et al., 2016; Bückner et al., 2018).

Generative properties

The CVAE is a generative model, and allows drawing random latent vectors $\mathbf{z} \sim \mathcal{N}(\mathbf{0}, \mathbf{I}_S)$ to decode them into artificial complex resistivity spectra. Figure 11 presents three such stochastic realizations, each scaled by a direct current resistivity ρ_0 chosen to emulate background resistivities spanning more than two orders of magnitude. The generated spectra consistently reproduce the qualitative signatures of SIP data, including a weak frequency dependence of the real component $\hat{\rho}'$ at low frequency, a gradual decrease of $\hat{\rho}'$ toward higher frequencies, and a dispersive peak in the imaginary component $-\hat{\rho}''$ associated with polarization relaxation.

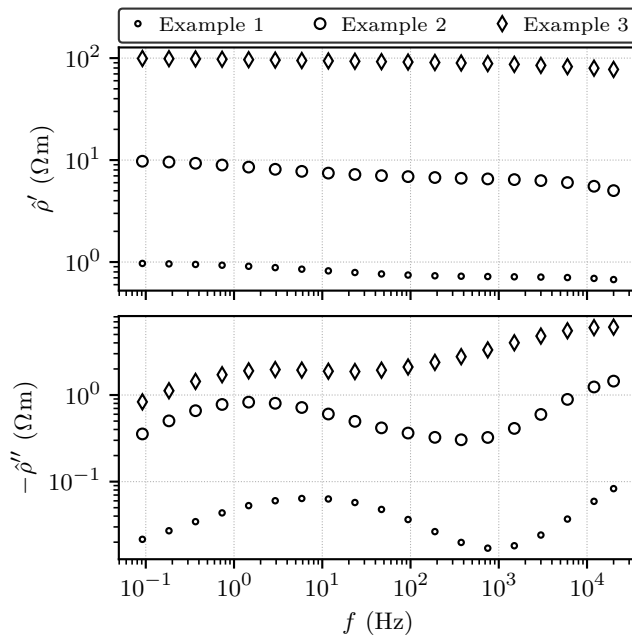


Figure 11: Examples of stochastic realizations sampled from the probabilistic decoder of the CVAE. Three random latent vectors are drawn and decoded to generate artificial SIP data. The top panel shows the real component $\hat{\rho}'$ as a function of frequency f and the bottom panel shows the negative imaginary component $-\hat{\rho}''$.

Example 1 in Figure 11 is a low-amplitude response, with ρ' varying between 0.71 and 1.02 $\Omega\text{ m}$ and $-\rho''$ between 1.8×10^{-2} and 8.7×10^{-2} $\Omega\text{ m}$. A distinct low-frequency relaxation peak is visible at 5.86 Hz, with a $-\hat{\rho}''$ of 6.7×10^{-2} $\Omega\text{ m}$. The associated half-maximum bandwidth spans nearly three orders of magnitude in frequency, which reflects a broad relaxation feature rather than a sharply defined single time constant. Example 2 is an intermediate-amplitude spectrum, with ρ' ranging from 5.3 to 10.3 $\Omega\text{ m}$ and $-\rho''$ between 0.32 and 1.52 $\Omega\text{ m}$. A low-frequency relaxation peak is detected at 1.46 Hz, with a substantially larger $-\hat{\rho}''$ of 8.7×10^{-1} $\Omega\text{ m}$. Example 3 produces a large-amplitude response, with ρ' between 79 and 102 $\Omega\text{ m}$ and $-\rho''$ spanning 0.85 to 6.23 $\Omega\text{ m}$. A low-frequency relaxation peak is present at 2.93 Hz, but its width cannot be resolved within the frequency grid, which suggests either a very broad relaxation or the superposition of multiple

characteristic times. We emphasize that these examples are purely artificial, yet data-driven. They reflect typical SIP patterns learned by the CVAE from the data set rather than actual polarization mechanisms. The spectra in Figure 11 therefore serve primarily as qualitative illustrations of the variability encoded in the latent space.

Model analysis

A detailed examination of parameter sensitivities, error patterns, and latent space organization provides insights into how the CVAE encodes and reconstructs SIP data.

Sensitivity analysis

Similarly to Bérubé and Baron (2023), we analyze the sensitivity structure of the selected CVAE model using its Jacobian (Figure 12). The Jacobian is computed for the end-to-end mapping from the input SIP spectra to the inferred RTD parameters, and therefore reflects the combined effects of the encoder, latent representation, and decoder. Two complementary measures are reported. The top panel in Figure 12 shows sensitivities with respect to the raw decoder outputs, which quantify the response of the model to absolute parameter perturbations and primarily reflect how the network allocates internal representational capacity prior to the enforcement of physical constraints. The bottom panel in Figure 12 shows elasticities, defined as derivatives with respect to the logarithm of the physical RTD parameters, which quantify output variations under multiplicative parameter changes and are therefore more directly interpretable in physical terms. In both cases, the indices are normalized to sum to 100%, which allows their relative importance to be compared.

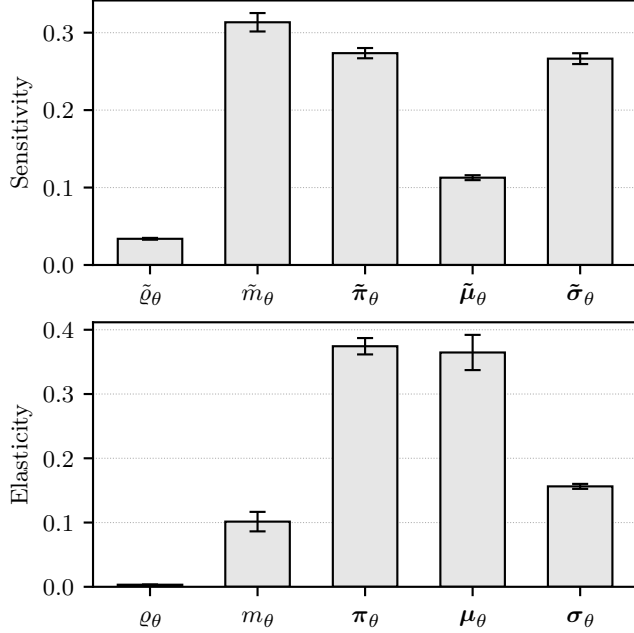


Figure 12: Relative parameter sensitivity structure of the CVAE. The top panel shows sensitivity indices computed from the Jacobian of the model with respect to the raw RTD parameters ($\tilde{\varrho}_\theta, \tilde{m}_\theta, \tilde{\pi}_\theta, \tilde{\mu}_\theta, \tilde{\sigma}_\theta$). The bottom panel shows elasticities computed with respect to the natural logarithm of the physical RTD parameters ($\varrho_\theta, m_\theta, \pi_\theta, \mu_\theta, \sigma_\theta$). Error bars denote the standard error across the data set.

The relative sensitivities of the raw RTD parameters indicate that the decoder is most responsive to perturbations in the mixture weights $\tilde{\pi}_\theta$ (27.4%), the mixture widths $\tilde{\sigma}_\theta$ (26.7%), and the total chargeability scale \tilde{m}_θ (31.3%). Together, these parameters account for approximately 85% of the total raw sensitivity. In contrast, the sensitivity to the relaxation time locations $\tilde{\mu}_\theta$ remains moderate (11.3%), while the sensitivity to the resistivity scaling parameter $\tilde{\varrho}_\theta$ is small (3.4%).

The relative elasticities of the physical RTD parameters reveal a different and more meaningful hierarchy. The largest elasticities correspond to the mixture weights π_θ (37.4%) and the relaxation time locations μ_θ (36.5%), followed by the mixture widths σ_θ (15.6%) and the total chargeability m_θ (10.1%). The elasticity associated with the resistivity scaling parameter ϱ_θ is small (0.3%). These results indicate that the CVAE relies predominantly on the placement and relative weighting of relaxation modes, rather than on global scaling parameters. The small relative elasticity of ϱ stems from the normalization of input data using Equation (15).

Error analysis

We evaluate the reconstruction accuracy of the CVAE using Equation (48). Across all frequencies and samples, the CVAE achieves low global reconstruction errors, with a NMAE of 0.66% for $|\rho|$, 0.53% for ρ' , 0.45% for ρ'' , and 0.24% for φ , on average. Figure 13 shows the frequency dependence

of the reconstruction error. For all components, the NMAE exhibits a smooth and systematic variation across the investigated frequency range. Errors are largest at the highest frequencies, reaching approximately 2.0% for $|\rho|$ and 1.4–1.5% for ρ' and ρ'' at 20 kHz, where capacitive coupling and instrumental effects typically limit the interpretability of SIP measurements. The error for φ also peaks in this range, with a NMAE close to 0.74%.

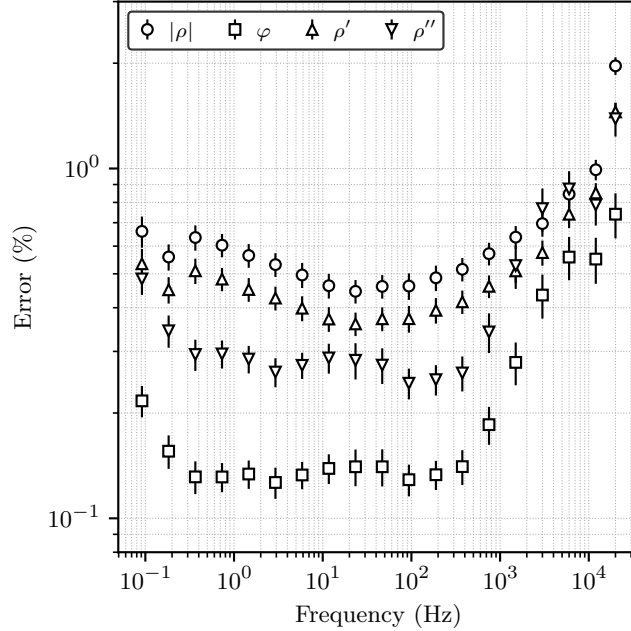


Figure 13: Frequency-dependent reconstruction error of the CVAE expressed as the NMAE. Errors are shown for the complex resistivity magnitude $|\rho|$, for its phase shift φ and for its real (ρ') and imaginary (ρ'') components. Error bars indicate the standard error of the mean across all samples.

As frequency decreases, reconstruction errors rapidly fall below 1% and remain nearly constant over most of the spectrum. In the low-frequency band between approximately 0.1 Hz and 1 kHz, which contains the dominant polarization features for the majority of samples, the NMAE stabilizes between 0.45 and 0.66% for $|\rho|$, 0.36 and 0.53% for ρ' , and 0.24 and 0.48% for ρ'' . Over the same range, φ is reconstructed with high accuracy, with NMAE values typically between 0.13 and 0.19%.

Latent space analysis

We investigate how the CVAE organizes SIP spectra internally by embedding the learned latent variables onto two dimensions using uniform manifold approximation and projection (UMAP; McInnes et al. 2018). The projection is applied to the posterior mean of the latent variables for each sample, without using any class labels during training or embedding. The resulting representation, shown in Figure 14, therefore reflects similarities learned only from the SIP data.

Distinct material groups form compact and well-organized clusters, which indicates that the latent variables encode significant differences in spectral shape and polarization behavior.

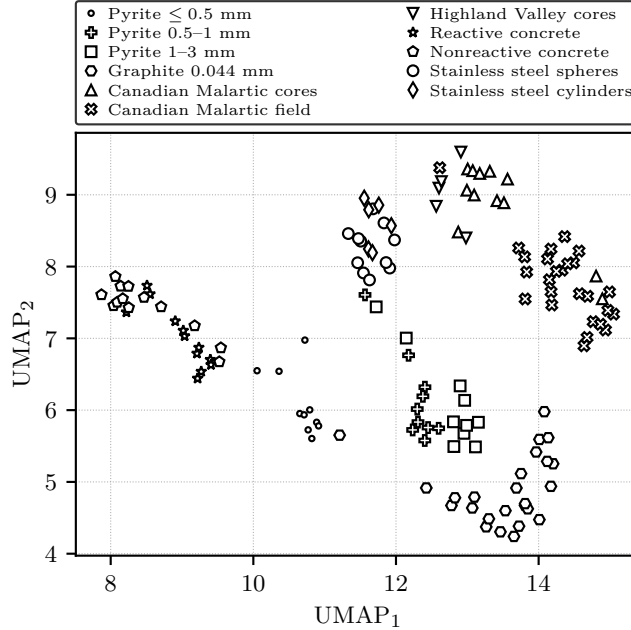


Figure 14: Two-dimensional UMAP embedding of the CVAE latent space. Each marker represents one SIP spectrum, with marker shapes denoting different sample groups. The embedding reveals well-organized clusters corresponding to material type and experimental conditions, despite the absence of sample labels during training.

The three pyrite grain-size series occupy neighboring but distinct regions of the latent space projection (Figure 14). As grain size increases, the cluster centroids shift systematically toward larger $UMAP_1$ values and slightly lower $UMAP_2$ values, while remaining relatively compact. This progression reflects consistent, size-dependent changes in the SIP response that are captured by the CVAE despite the absence of explicit grain-size information. Graphite mixtures form a broader cluster centered at lower $UMAP_1$ and higher $UMAP_2$ values, with a larger spread than the pyrite series. This wider dispersion is consistent with the variability observed in graphite SIP signatures (Figure 9).

Natural rock samples also exhibit coherent grouping. Canadian Malartic core and field measurements form adjacent but distinct clusters, with field data shifted toward higher $UMAP_1$ and lower $UMAP_2$ values. This separation likely reflects differences in acquisition conditions and noise characteristics rather than fundamental changes in polarization mechanisms. Highland Valley core samples cluster near those of Canadian Malartic with relatively small spread.

The two concrete data sets occupy the left portion of the embedding, with reactive and nonreactive concretes forming neighboring clusters. Their proximity reflects similar spectral responses,

while the systematic offset between centroids suggests that the latent space captures subtle but repeatable differences related to chemical reactivity.

Clustering metrics

The clustering metrics reported in Table 4 confirm that the latent representation learned by the CVAE provides a markedly improved separation of the sample groups compared with conventional RTD parameters. When clustering is performed in the m and $\bar{\tau}$ parameter space, the silhouette score remains low (0.068), indicating overlap between groups. In contrast, the UMAP projection of the latent space yields a higher silhouette score (0.256), which indicates better-defined and more compact clusters. As further evidence of enhanced clustering in the latent space embedding, the Davies–Bouldin index decreases from 5.537 in the RTD parameter space to 1.980 in the latent projection, and the Calinski–Harabasz index increases from 60.6 to 162.7.

Feature space	Silhouette	Davies–Bouldin	Calinski–Harabasz
Debye RTD parameters	0.068	5.537	60.6
Latent space projection	0.256	1.980	162.7

Table 4: Clustering metrics for RTD parameters and UMAP latent projection. Boldface highlights the best score for each metric.

Results in Table 4 clearly demonstrate that the CVAE latent variables encode discriminative information about SIP spectra that is not captured by summary parameters such as total chargeability and mean relaxation time alone. Importantly, this improved separability does not imply that individual latent dimensions correspond to specific physical parameters. Rather, the latent space represents a nonlinear combination of spectral features that collectively capture polarization amplitude, characteristic timescales, and dispersion patterns. The UMAP embedding therefore provides a new exploratory tool for identifying similarities and contrasts among SIP responses, and is complementary to traditional RTD interpretation.

DISCUSSION

Machine learning inversion

The proposed approach should not be interpreted as a predictive model in the supervised machine learning sense. The paradigm of train–validation–test partitioning does not apply because the CVAE is trained as an unsupervised machine learning model on the full data set and because the goal is not to generalize to unseen data. If the objective is to obtain the RTD parameters

of a particular SIP measurement, the model can be trained using that spectrum alone. In this setting, the CVAE acts as a regularized nonlinear solver. Alternatively, the CVAE may be trained on a curated subset of spectra or on larger, heterogeneous, SIP data collections to extract the discriminant features that characterize broader classes of geological materials.

Advantages

Ambiguity and regularization

Ambiguity is a well-known property of the DD approach. In fact, several distinct RTD can reproduce the same complex resistivity spectrum, and conventional inversions usually impose smoothness constraints to obtain stable and unique solutions (e.g., Nordsiek and Weller, 2008; Florsch et al., 2014; Weigand and Kemna, 2016). With Markov-chain Monte Carlo methods, the RTD is typically reparameterized with a polynomial function because there are too many parameters to solve for otherwise (Keery et al., 2012; Bérubé et al., 2017). One must then select the polynomial order, typically between second and fifth order, and this choice becomes an additional hyperparameter that depends on the data and influences the solution.

The CVAE handles ambiguity and regularization through its latent space and a Gaussian mixture model. Conceptually, this leads to a more physically consistent formulation, since the recovered distribution is continuous and learned from the data, rather than by an externally imposed polynomial model and a predefined grid. First, the Gaussian mixture formulation yields a continuous RTD, even when the spectra contain multiple or overlapping polarization processes. Second, the stochastic decoder produces many admissible RTD for a single spectrum because each latent sample yields a valid solution (e.g., Figure 6). This ensemble of realizations defines a probability density over the RTD rather than a single deterministic model.

Unified data set inversion

The CVAE operates at the data set level and fits all spectra at once. This unified representation provides access to information that spectrum-by-spectrum inversions cannot supply. Specifically, the CVAE encodes low-dimensional and physically meaningful descriptors of complex resistivity dispersion. This enables tasks such as clustering (Figure 14), discrimination between material classes (Figure 7), and sensitivity analysis (Figure 12). The CVAE therefore doubles as an exploratory tool that reveals the structure of SIP data sets in addition to recovering RTD parameters.

Complex-valued representation

A key difference between our approach and, to the best of our knowledge, all other existing SIP decomposition frameworks, is that the CVAE operates directly in the complex domain. SIP data satisfy Kramers–Kronig relationships, and their real and imaginary parts are strongly coupled. Instead of separating the real and imaginary parts and treating them as independent regression targets, the CVAE uses a complex-valued input representation and objective function, which ensures that amplitude and phase information are propagated jointly in the inverse mapping from $\rho(\omega)$ to $\gamma(\tau)$. This choice is motivated not only by physics, but also by evidence that complex-valued neural networks offer measurable performance gains in SIP parameter estimation when compared with their real-valued counterparts (Bérubé et al., 2025).

Limitations

Model selection and performance

The CVAE performance depends on design choices such as the size of the latent space, the number of Gaussian mixture components, and the depth and size of the encoder–decoder networks. Although the model selection procedure mitigates this sensitivity, suboptimal choices can lead to underfitting or an over-regularized latent space. In particular, the use of a relatively large mixture dimension ($N = 128$) compared to the size of each spectra ($K = 19$) raises the potential risk of overfitting. However, the model selection results (Figures 2 and 3) and the stability of the training dynamics and reconstruction accuracy across repetitions (Figure 4) suggest that the selected architecture remains well constrained by the data.

Moreover, reaching a good balance between \mathcal{L}_{NLL} , which controls curve fitting quality, and D_{KL} , which controls regularization and expressibility of the generative model, is not a trivial task (e.g., Higgins et al., 2017). Rather than manually tuning the balance between both terms, we instead use the calibrated decoder formulation of Rybkin et al. (2021) by explicitly considering the data uncertainty. Therefore, input data quality has a strong influence on the performance of the CVAE.

Latent space interpretation

Although the latent space captures meaningful variations in SIP data (Figure 14), its axes do not correspond directly to physical parameters. The connection between latent variables and polarization characteristics is empirical. As such, the latent space may be used for clustering, but its axes should be interpreted cautiously.

Computational cost

Although CVAE inference is fast (2.3 ± 0.2 ms for one forward operation on a batch of 140 spectra, or 131 ± 1 μ s for one spectrum, using the Apple M5 chip), the training procedure itself requires more computation time than linear or nonlinear DD. In this work, optimizing the CVAE on the full data set takes approximately three minutes. Fitting only one spectrum with the CVAE reduces training time to about 0.8 s. However, this mode of operation does not provide a meaningful latent space representation because the model cannot learn variability from a single example.

Generalization capabilities

As discussed previously, the CVAE is an unsupervised model. This choice is primarily motivated by the limited size of the data set ($J = 140$ spectra), which restricts the feasibility of supervised training. Given a substantially larger and more diverse SIP data collection (e.g., several thousand spectra), it would be possible to train, validate and test a supervised variant of the CVAE as a fast Debye decomposition inference model for unseen data, with the computational cost incurred primarily during training. Such an extension would, however, be strongly conditioned by the representativity of the training set. In particular, unseen SIP spectra whose relaxation modes fall outside the bounds defined by Equations (29)–(30) during training would constitute out-of-distribution cases and could lead to biased or truncated RTD estimates at inference time. Addressing this limitation would likely require training data spanning broader frequency ranges, or introducing mechanisms for detecting out-of-distribution spectra, which are beyond the scope of the present work.

CONCLUSIONS

We set out to formalize DD as a probabilistic machine learning problem and to evaluate whether a CVAE can provide an effective and interpretable inverse mapping from SIP data to a continuous RTD. The results demonstrate that these objectives are met. First, the CVAE learns a stable inverse operator that reconstructs SIP data with relatively low error across the 90 mHz to 20 kHz range, while providing physically plausible stochastic realizations. Second, the decoder yields continuous RTD from which total chargeability, peak relaxation times, and mean relaxation time can be extracted and quantitatively related to grain size, volumetric fraction, and material type. Third, the CVAE performs the inversion on the entire data set rather than on individual spectra. This formulation yields a latent representation that captures common structure across samples while preserving sample-specific variability. The latent variables thus organize the data into a structured space in which sample populations cluster naturally, without supervision, and with

significantly improved separability relative to conventional RTD parameters. The integration of machine learning into SIP data processing workflows is a promising avenue for both laboratory studies and field investigations. Future work should extend this framework to field-scale or time-lapse studies across varying lithologies or temporal events, respectively. Reformulating the CVAE to learn from known data labels may also grant interesting conditional generative properties to the model.

APPENDIX A

COMPLEX-VALUED LIKELIHOOD

The complex-valued likelihood adopted in this work is a scalar specialization of the second-order complex Gaussian distribution (Picinbono, 1996). Let $\eta \in \mathbb{C}$, the SIP data residuals, denote a zero-mean complex random variable. We omit the frequency indices for clarity. Its second-order statistics are characterized by the variance

$$v = \mathbb{E}[|\eta|^2], \quad (\text{A-1})$$

and the pseudo-variance

$$\delta = \mathbb{E}[\eta^2]. \quad (\text{A-2})$$

Following Picinbono (1996), we define the augmented random vector

$$\underline{\eta} = \begin{bmatrix} \eta \\ \eta^* \end{bmatrix}, \quad (\text{A-3})$$

whose augmented covariance matrix reads

$$\underline{\mathbf{C}} = \mathbb{E}[\underline{\eta}\underline{\eta}^{\text{H}}] = \begin{bmatrix} v & \delta \\ \delta^* & v \end{bmatrix}. \quad (\text{A-4})$$

Positive definiteness of $\underline{\mathbf{C}}$ requires $v > |\delta|$.

The probability density function of η is then given by

$$p(\eta) = \frac{1}{\pi \sqrt{\det(\underline{\mathbf{C}})}} \exp\left(-\frac{1}{2} \underline{\eta}^{\text{H}} \underline{\mathbf{C}}^{-1} \underline{\eta}\right). \quad (\text{A-5})$$

For the scalar case, the determinant and inverse of $\underline{\mathbf{C}}$ are

$$\det(\underline{\mathbf{C}}) = v^2 - |\delta|^2, \quad (\text{A-6})$$

and

$$\underline{\mathbf{C}}^{-1} = \frac{1}{v^2 - |\delta|^2} \begin{bmatrix} v & -\delta \\ -\delta^* & v \end{bmatrix}. \quad (\text{A-7})$$

The quadratic form in the exponent of Equation (A-5) is thus

$$\underline{\eta}^H \underline{\mathbf{C}}^{-1} \underline{\eta} = \frac{1}{v^2 - |\delta|^2} \begin{bmatrix} \eta^* & \eta \end{bmatrix} \begin{bmatrix} v & -\delta \\ -\delta^* & v \end{bmatrix} \begin{bmatrix} \eta \\ \eta^* \end{bmatrix} \quad (\text{A-8})$$

$$= \frac{1}{v^2 - |\delta|^2} \left(2v|\eta|^2 - \delta(\eta^*)^2 - \delta^*\eta^2 \right) \quad (\text{A-9})$$

$$= \frac{2}{v^2 - |\delta|^2} \left(v|\eta|^2 - \Re\{\delta^*\eta^2\} \right). \quad (\text{A-10})$$

Substituting these results into Equation (A-5) yields the scalar density

$$p(\eta; v, \delta) = \frac{1}{\pi\sqrt{v^2 - |\delta|^2}} \exp\left(-\frac{v|\eta|^2 - \Re\{\delta^*\eta^2\}}{v^2 - |\delta|^2}\right). \quad (\text{A-11})$$

REFERENCES

- Attwa, M., and T. Günther, 2013, Spectral induced polarization measurements for predicting the hydraulic conductivity in sandy aquifers: *Hydrology and Earth System Sciences*, **17**, 4079–4094; doi: 10.5194/hess-17-4079-2013.
- Bairlein, K., A. Hördt, and S. Nordsiek, 2014, The influence on sample preparation on spectral induced polarization of unconsolidated sediments: *Near Surface Geophysics*, **12**, 667–678; doi: <https://doi.org/10.3997/1873-0604.2014023>.
- Benzetta, R., 2024, Caractérisation géoélectrique du graphite naturel et application à l’exploration minérale: Master’s thesis, Polytechnique Montréal.
- Breede, K., A. Kemna, O. Esser, E. Zimmermann, H. Vereecken, and J. Huisman, 2012, Spectral induced polarization measurements on variably saturated sand-clay mixtures: *Near Surface Geophysics*, **10**, 479–489; doi: <https://doi.org/10.3997/1873-0604.2012048>.
- Bérubé, C. L., and F. Baron, 2023, Bayesian inference of petrophysical properties with generative spectral induced polarization models: *Geophysics*, **88**, E79–E90; doi: 10.1190/geo2022-0495.1.
- Bérubé, C. L., M. Chouteau, P. Shamsipour, R. J. Enkin, and G. R. Olivo, 2017, Bayesian inference of spectral induced polarization parameters for laboratory complex resistivity measurements of rocks and soils: *Computers & Geosciences*, **105**, 51–64; doi: 10.1016/j.cageo.2017.05.001.
- Bérubé, C. L., S. Gagnon, E. R. Kenko, J.-L. Gagnon, L. M. A. Nagasingha, R. Ghanati, and F. Baron, 2025, Complex-valued neural networks for spectral induced polarization applications: *Geophysical Journal International*, **243**, ggaf348; doi: 10.1093/gji/ggaf348.
- Bérubé, C. L., G. R. Olivo, M. Chouteau, and S. Perrouty, 2019, Mineralogical and textural controls on spectral induced polarization signatures of the Canadian Malartic gold deposit: Applications to mineral exploration: *Geophysics*, **84**, B135–B151; doi: 10.1190/geo2018-0404.1.
- Bücker, M., A. F. Orozco, and A. Kemna, 2018, Electrochemical polarization around metallic particles — Part 1: The role of diffuse-layer and volume-diffusion relaxation: *Geophysics*, **83**, E203–E217; doi: 10.1190/geo2017-0401.1.
- Flores Orozco, A., A. Kemna, C. Oberdörster, L. Zschornack, C. Leven, P. Dietrich, and H. Weiss, 2012, Delineation of subsurface hydrocarbon contamination at a former hydrogenation plant using spectral induced polarization imaging: *Journal of Contaminant Hydrology*, **136-137**, 131–144; doi: 10.1016/j.jconhyd.2012.06.001.
- Florsch, N., A. Revil, and C. Camerlynck, 2014, Inversion of generalized relaxation time distributions with optimized damping parameter: *Journal of Applied Geophysics*, **109**, 119–132; doi: 10.1016/j.jappgeo.2014.07.013.
- Gao, Z., F.-H. Haegel, J. A. Huisman, O. Esser, E. Zimmermann, and H. Vereecken, 2017, Spectral induced polarization for the characterisation of biochar in sand: *Near Surface Geophysics*, **15**, 645–656; doi: 10.3997/1873-0604.2017045.
- Grenon, C., 2018, Caractérisation pétrophysique du gisement cuprifère de Highland Valley

- (Colombie-Britannique): Master's thesis, École Polytechnique de Montréal.
- Gurin, G., A. Tarasov, Y. Ilyin, and K. Titov, 2013, Time domain spectral induced polarization of disseminated electronic conductors: Laboratory data analysis through the Debye decomposition approach: *Journal of Applied Geophysics*, **98**, 44–53; doi: 10.1016/j.jappgeo.2013.07.008.
- Gurin, G., A. Tarasov, Y. Il'in, and K. Titov, 2015a, Application of the Debye decomposition approach to analysis of induced-polarization profiling data (Julietta gold-silver deposit, Magadan Region): *Russian Geology and Geophysics*, **56**, 1757–1771; doi: 10.1016/j.rgg.2015.11.008.
- Gurin, G., K. Titov, Y. Ilyin, and A. Tarasov, 2015b, Induced polarization of disseminated electronically conductive minerals: a semi-empirical model: *Geophysical Journal International*, **200**, 1555–1565; doi: 10.1093/gji/ggu490.
- Hase, J., G. Gurin, K. Titov, and A. Kemna, 2023, Conversion of Induced Polarization Data and Their Uncertainty from Time Domain to Frequency Domain Using Debye Decomposition: *Minerals*, **13**; doi: 10.3390/min13070955.
- Higgins, I., L. Matthey, A. Pal, C. Burgess, X. Glorot, M. Botvinick, S. Mohamed, and A. Lerchner, 2017, beta-vae: Learning basic visual concepts with a constrained variational framework: Presented at the International Conference on Learning Representations.
- Holtz, R. D., and W. D. Kovacs, 1981, *An introduction to geotechnical engineering*: Prentice-Hall.
- Keery, J., A. Binley, A. Elshenawy, and J. Clifford, 2012, Markov-chain Monte Carlo estimation of distributed Debye relaxations in spectral induced polarization: *Geophysics*, **77**, E159–E170; doi: 10.1190/geo2011-0244.1.
- Khajehnouri, Y., M. Chouteau, P. Rivard, and C. L. Bérubé, 2019, Measuring electrical properties of mortar and concrete samples using the spectral induced polarization method: laboratory setup: *Construction and Building Materials*, **210**, 1–12; doi: 10.1016/j.conbuildmat.2019.03.160.
- Khajehnouri, Y., M. Chouteau, P. Rivard, and C. L. Bérubé, 2020a, Non-destructive non-invasive assessment of the development of alkali-silica reaction in concrete by spectral induced polarization: Evaluation of the complex electrical properties: *Construction and Building Materials*, **238**, 117719; doi: 10.1016/j.conbuildmat.2019.117719.
- Khajehnouri, Y., P. Rivard, M. Chouteau, and C. L. Bérubé, 2020b, Validation of complex electrical properties of concrete affected by accelerated alkali-silica reaction: *Cement and Concrete Composites*, **113**, 103660; doi: 10.1016/j.cemconcomp.2020.103660.
- Kingma, D. P., and J. Ba, 2015, Adam: A Method for Stochastic Optimization: 3rd International Conference on Learning Representations, ICLR 2015, San Diego, CA, USA, May 7-9, 2015, Conference Track Proceedings, 8024–8035.
- Kingma, D. P., and M. Welling, 2014, Auto-Encoding Variational Bayes: 2nd International Conference on Learning Representations, ICLR 2014, Banff, AB, Canada, April 14-16, 2014, Conference Track Proceedings, 1–14.
- Martin, T., A. Weller, and L. Behling, 2021, Desaturation effects of pyrite–sand mixtures on induced polarization signals: *Geophysical Journal International*, **228**, 275–290; doi:

10.1093/gji/ggab333.

- McInnes, L., J. Healy, N. Saul, and L. Großberger, 2018, UMAP: Uniform Manifold Approximation and Projection: *Journal of Open Source Software*, **3**, 861; doi: 10.21105/joss.00861.
- Misra, S., C. Torres-Verdín, A. Revil, J. Rasmus, and D. Homan, 2016, Interfacial polarization of disseminated conductive minerals in absence of redox-active species — Part 1: Mechanistic model and validation: *Geophysics*, **81**, E139–E157; doi: 10.1190/geo2015-0346.1.
- Morgan, F. D., and D. P. Lesmes, 1994, Inversion for dielectric relaxation spectra: *The Journal of Chemical Physics*, **100**, 671–681; doi: 10.1063/1.466932.
- Nordsiek, S., and A. Weller, 2008, A new approach to fitting induced-polarization spectra: *Geophysics*, **73**, F235–F245; doi: 10.1190/1.2987412.
- Paszke, A., S. Gross, F. Massa, A. Lerer, J. Bradbury, G. Chanan, T. Killeen, Z. Lin, N. Gimelshein, L. Antiga, A. Desmaison, A. Kopf, E. Yang, Z. DeVito, M. Raison, A. Tejani, S. Chilamkurthy, B. Steiner, L. Fang, J. Bai, and S. Chintala, 2019, PyTorch: An Imperative Style, High-Performance Deep Learning Library, *in* *Advances in Neural Information Processing Systems 32*: Curran Associates, Inc., 8024–8035.
- Picinbono, B., 1996, Second-order complex random vectors and normal distributions: *IEEE Transactions on Signal Processing*, **44**, 2637–2640; doi: 10.1109/78.539051.
- Revil, A., 2013, On charge accumulation in heterogeneous porous rocks under the influence of an external electric field: *Geophysics*, **78**, D271–D291; doi: 10.1190/geo2012-0503.1.
- Revil, A., N. Florsch, and C. Camerlynck, 2014, Spectral induced polarization porosimetry: *Geophysical Journal International*, **198**, 1016–1033; doi: 10.1093/gji/ggu180.
- Rybkin, O., K. Daniilidis, and S. Levine, 2021, Simple and Effective VAE Training with Calibrated Decoders: *Proceedings of the 38th International Conference on Machine Learning*, PMLR, 9179–9189.
- Seigel, H. O., 1959, Mathematical formulation and type curves for induced polarization: *Geophysics*, **24**, 547–565.
- Sohn, K., H. Lee, and X. Yan, 2015, Learning Structured Output Representation using Deep Conditional Generative Models: Presented at the *Advances in Neural Information Processing Systems*, Curran Associates, Inc.
- Ustra, A., C. A. Mendonça, D. Ntarlagiannis, and L. D. Slater, 2016, Relaxation time distribution obtained from a Debye decomposition of spectral induced polarization data: *Geophysics*, **81**, E129–E138; doi: 10.1190/geo2015-0095.1.
- Ustra, A., L. Slater, D. Ntarlagiannis, and V. Elis, 2012, Spectral Induced Polarization (SIP) signatures of clayey soils containing toluene: *Near Surface Geophysics*, **10**, 503–515; doi: <https://doi.org/10.3997/1873-0604.2012015>.
- Virtue, P., S. X. Yu, and M. Lustig, 2017, Better than real: Complex-valued neural nets for MRI fingerprinting: *2017 IEEE International Conference on Image Processing (ICIP)*, 3953–3957. (ISSN: 2381-8549).

- Volkman, J., and N. Klitzsch, 2015, Wideband impedance spectroscopy from 1 mHz to 10 MHz by combination of four- and two-electrode methods: *Journal of Applied Geophysics*, **114**, 191–201; doi: 10.1016/j.jappgeo.2015.01.012.
- Weigand, M., and A. Kemna, 2016, Debye decomposition of time-lapse spectral induced polarisation data: *Computers & Geosciences*, **86**, 34–45; doi: 10.1016/j.cageo.2015.09.021.
- Weller, A., S. Nordsiek, and W. Debschütz, 2010a, Estimating permeability of sandstone samples by nuclear magnetic resonance and spectral-induced polarization: *Geophysics*, **75**, E215–E226; doi: 10.1190/1.3507304.
- Weller, A., L. Slater, and S. Nordsiek, 2013, On the relationship between induced polarization and surface conductivity: Implications for petrophysical interpretation of electrical measurements: *Geophysics*, **78**, D315–D325; doi: 10.1190/geo2013-0076.1.
- Weller, A., L. Slater, S. Nordsiek, and D. Ntarlagiannis, 2010b, On the estimation of specific surface per unit pore volume from induced polarization: A robust empirical relation fits multiple data sets: *Geophysics*, **75**, WA105–WA112; doi: 10.1190/1.3471577.
- Yager, W. A., 1936, The Distribution of Relaxation Times in Typical Dielectrics: *Physics*, **7**, 434–450; doi: 10.1063/1.1745355.
- Zibulski, E., and N. Klitzsch, 2023, Influence of Inner Surface Roughness on the Spectral Induced Polarization Response—A Numerical Study: *Journal of Geophysical Research: Solid Earth*, **128**, e2022JB025548; doi: 10.1029/2022JB025548.
- Zisser, N., A. Kemna, and G. Nover, 2010, Dependence of spectral-induced polarization response of sandstone on temperature and its relevance to permeability estimation: *Journal of Geophysical Research: Solid Earth*, **115**; doi: 10.1029/2010JB007526.
- Zorin, N., 2015, Spectral induced polarization of low and moderately polarizable buried objects: *Geophysics*, **80**, E267–E276; doi: 10.1190/geo2014-0154.1.